ZANCO Journal of Pure and Applied Sciences

TYPE Original article
DOI http://dx.doi.org/10.21271/ZJPAS.37.4.5

OPEN ACCESS

*Corresponding author

Heman Abdulkhaleq A. Gaznayee
heman.ahmed@su.edu.krd

RECEIVED :01 /03 /2025
ACCEPTED :13/04/ 2025
PUBLISHED :31/08/ 2025

KEYWORDS:

Remote Sensing, Environmental Stress, Forest Degradation, and Amedi District.

A Comprehensive Remote Sensing Approach for Assessing Forest Degradation and Environmental Stress in Amedi District, Kurdistan Region of Iraq

Nofa Bahzad Mohammed Alsinayi[1], Mohammed Hadeat Obeyed Alzuhary[1] and Heman Abdulkhaleq A. Gaznayee [2*]

1Department of Forestry, College of Agricultural Engineering Sciences, University of Duhok, Duhok, Kurdistan Region, Iraq
2Department of Forestry, College of Agriculture Engineering Sciences, Salahaddin University-Erbil, Erbil Kurdistan Region, Iraq

ABSTRAC

Forest ecosystems in Amedi district face stress from conflict, fires, climate variability, and unsustainable land use. This study uses remote sensing and geospatial techniques to assess forest degradation from 2000 to 2024. Modified Soil-Adjusted Vegetation Index (MSAVI2), Normalized Difference Vegetation Index (NDVI), Land Surface Temperature (LST), and Normalized Difference Moisture Index (NDMI) data are used to measure changes in forest land (FL) and non-forested land (NFL), NDMI, and LST. The results obtained from NDVI data reveal inadequate regeneration rates to counterbalance the total forest loss, while non-forest regions have significantly increased from 5.8% (160.8 km²) to 19.7% (546.6 km²). NDVI-based FL dropped from 90.3% (2505.3 km²) to 73.3% (2032.2 km²), and MSAVI2-based FL declined from 86.3% (2393.3 km²) to 74.3% (2062.3 km²). Conversely, NDVI also indicated an increase in degraded land cover, especially during 2013–2015 and 2020–2024. The LST class (<35°C) declined from 849 km² to 520 km², while the High (45–50°C) and Extreme (>50°C) LST zones exhibited a marked expansion. Mann-Kendall tests revealed significant temporal changes in NDVI, MSAVI2, NDMI, and LST ($Z > \pm 1.96$). Sen's slope quantified trends; Pearson's correlation confirmed strong vegetation/climate stress links ($r > 0.7$, $p < 0.05$). The Mann-Kendall trend test confirmed a significant upward LST trend ($\tau = 0.312$, $p = 0.034$), with a Sen's slope of 14.662 km² per unit time. Trend detection using the non-parametric Mann-Kendall test validated significant changes across variables without assuming normality. The ARIMA (1,0,0) model forecasts a continued decline through the projection horizon. Forecast intervals widen at a 95% confidence level due to uncertainty in a near-unit root process. The forecast error measured by MAPE is about 5.0%, showing moderate reliability. ARIMA models further revealed robust forecasting capability for environmental indicators, validating model assumptions with stationary residuals and minimal error. For the NDVI-derived forest area, a negative trend was identified (Sen's slope = –22 km²/unit time, $p < 0.0001$), confirming ongoing deforestation. Pearson correlation analysis showed strong associations between vegetation indices and temperature/moisture variables ($r > 0.7$, $p < 0.05$). Although robust, these relationships may be influenced by confounding factors such as climate change, forest degradation, forest fires, armed conflict, and broader land use and land cover changes. Findings emphasize conservation strategies to combat deforestation, warming trends, and safeguard ecosystem resilience.

1.Introductio

Forests are crucial ecosystems providing many ecological, economic, and social benefits. They serve as carbon sinks, regulate the hydrological cycle, and support biodiversity while offering resources for local and indigenous communities (Köhl et al., 2015). However, forest ecosystems across the globe face increasing pressures from anthropogenic activities, climate change, and geopolitical conflicts. In regions such as Iraq's border districts with Turkey, forests have been significantly impacted by climate variability, prolonged conflict, and human-induced degradation, necessitating urgent scientific assessment and conservation measures (Jaff, 2023).

Rising temperatures, decreased precipitation, and prolonged droughts are all signs of climate change in Iraq (Heman Abdulkhaleq A Gaznayee et al., 2022). Environmental changes have an unfavorable effect on forest regeneration, water availability, and soil moisture, making forest ecosystems more vulnerable(Kumar, Kumar, and Saikia, 2022). Duhok, located in northern Iraq's semiarid zone, is witnessing major climatic change. According to studies, the region's temperature has steadily increased over the last few decades, but yearly rainfall has decreased (Eklund and Seaquist, 2015). Climate change has raised evapotranspiration rates, reduced soil fertility, and made forests more vulnerable to flames. A large proportion of Dohuk locals depend on trees for fuel, grazing, and non-timber forest products (Mohammad and Lojka, 2018). As forest resources decrease due to climate change, people resort to alternative management techniques such as excessive logging and agricultural land conversion, accelerating forest degradation (Basu, 2011). The effectiveness of remote sensing in monitoring Iraqi forest dynamics has been demonstrated by recent studies. Al-Hamdan et al. (2017) assessed deforestation changes in the Kurdistan area using Landsat satellite images and found a concerning decline in forest cover over the last 20 years (Hamad et al., 2017).

The geographical location and topographic diversity induce a climate variation over Iraq(Beg and Al-Sulttani, 2020). In Iraq's Kurdistan Region, the province of Duhok is located where many environmental stresses converge. The area preserves a range of woodlands that have historically supported biodiversity and local livelihoods (Kollert et al., 2014). These Forests have seen severe deterioration in recent decades, which has been linked to war-related activities, armed conflict, and climate (Abdulwahid et al., 2021). Significant negative effects on the ecosystem are caused by the continuous loss of forest cover, including reduced carbon sequestration, increased soil erosion, desertification, and the loss of endemic species' habitats. According to the study by Habeeb and Mustafa (2025), environmental factors play a crucial role in influencing the distribution of forest cover, and the effectiveness of advanced deep learning techniques in environmental modeling is demonstrated. Their analysis predicts a significant reduction in forest cover, decreasing from 364.17 km² in 2000 to 240.50 km² by 2022. These findings emphasize the substantial influence of environmental variables on forest dynamics and highlight the powerful capabilities of advanced deep learning methods in forecasting and elucidating environmental transformations(Habeeb and Mustafa, 2024). According to the study, Vilanova et al (2020), the Autoregressive Integrated Moving Average (ARIMA) model was utilized to evaluate past and predict future vegetation activity in Amazonas, Brazil, from 2001 to 2018. This assessment incorporated variables such as air temperature, rainfall, soil moisture, fire foci, land surface temperature, the Normalized Difference Vegetation Index (NDVI), and the Vegetation Health Index (VHI)(Vilanova et al., 2020).

In this area of study, remote sensing and geoinformatics are helpful tools because they provide precise information about changes in land cover and the health of forests (Liu et al., 2014). According to Borrelli et al.(2020), remote sensing is the process of analyzing environmental changes over time using imagery from satellites and aerial data. Spatial analytic skills are enhanced by geoinformatics, which combines remote sensing data with geographic information systems (GIS). (Gabriele et al.(2023)state that GIS-based models can predict the likelihood of

deforestation risks, determine how changes in temperature impact forest cover, and assist in forest management decision-making. Geospatial research in the Duhok districts may help direct targeted conservation efforts and offer important insights into the spatial pattern of forest degradation (Ismael, 2015). To identify deforestation, assess changes in vegetation growth, and assess the effects of environmental disturbances like drought and wildfires, NDVI is commonly used in forest monitoring (Pettorelli et al., 2005). An increased danger of forest fires, reduced evaporation and transpiration, and water stress in plants are all frequently indicated by high LST values (Li et al., 2013). Understanding how land surface temperature and vegetation interact is crucial to understanding the carbon cycle since temperature variations affect forest respiration, transpiration, and photosynthesis(Zhao and Running, 2010).

An essential spectral index for determining vegetation moisture is the NDMI. Low NDMI levels are indicative of water stress, forest degradation, or deforestation. Healthy vegetation with adequate precipitation is indicated by high scores. NDMI is widely used to monitor deforestation brought on by changes in land use, identify drought, and evaluate post-fire recovery (Bousquet et al., 2022). In remote sensing applications, LST, NDMI, NDVI, and MSAVI2 are frequently used to track forests on a local and global level. High-resolution data from satellites like Landsat and Sentinel-2 may be used to identify changes in the temperature, moisture content, and health of the forest's plants (Roy et al., 2005). Wang et al (2024) develops a system based on deep learning to inspect and confirm new deforestation sites using high-resolution satellite imagery. The approach aims to automate the validation process, addressing challenges associated with manual inspection, and enhancing the accuracy of deforestation monitoring(Wang et al., 2024). The integration of machine learning (ML) with remote sensing technologies has revolutionized environmental monitoring, particularly in the accurate detection and analysis of deforestation. Recent studies by Habeeb and Mustafa (2025) examines the spatiotemporal dynamics of forest cover in Duhok district, Iraq, where urbanization, industrial activities, and agricultural expansion have significantly impacted the environment. Utilizing an Ensemble Deep Learning approach, the study integrated Land Use and Land Cover data and environmental factors (climate, topography, and geology) to model forest cover changes from 2000 to 2060. The findings highlight the critical role of environmental factors in shaping forest cover distribution and demonstrate the efficacy of advanced deep learning techniques in environmental modeling(Habeeb and Mustafa, 2024).

A more accurate way to assess environmental stress and forest health is to combine LST, NDMI, NDVI, and MSAVI2. Severe drought, heightened fire risk, and environmental deterioration are often indicated by a high LST paired with a low NDMI (Kalluri et al., 2021). While MSAVI2 aids in identifying vegetation cover in areas where soil influences conventional vegetation indices, NDVI enhances NDMI by offering data on the greenness of vegetation. By combining these indicators, it is possible to further examine how climate change affects forests, including variations in temperature, moisture content, and vegetation density (Gu et al., 2008). Early warning systems for droughts, wildfires, and deforestation are made easier by the integration of these factors, which is particularly advantageous for remote sensing in forest management and conservation (Nemani et al., 2003).

This study examines the relationship between environmental degradation and governance to assess forest degradation and environmental stress in the Amedi district in light of the Sustainable Development Goals of the UN. Under SDG 15, the goal is to use satellite imagery and GIS analysis to evaluate the Amedi district's forest deterioration. The goal is to assess the role of Environmental stress in forest decline by analyzing LST and NDMI variability exacerbating droughts, wildfires, and forest stress, impacting vegetation health (SDG 13). Research highlights the essential role of forests in mitigating climate change, supporting ecosystems, and fostering environmental balance, providing insights for

decision-makers and stakeholders in pursuit of enduring sustainability.

2. Materials and Methods

2.1. Study Area

The research was conducted in Duhok Governorate (DU), Amadiya district. The soil in the area is categorized as non-saline(Eklund, 2012; Mustafa and Noori, 2013). DU's climate mirrors that of the Mediterranean, characterized by moderate to chilly and damp winters and warm to scorching and arid summers. The average yearly temperature ranges from 19.3°C to 21.2°C, with winter temperatures spanning from 0°C to 15°C and summer temperatures from 20°C to 37°C (Figures 1 and 2. Precipitation data were acquired from the Ministry of Agriculture and Water Resources and the General Directorate of Water Resources in Iraq. Temperature and relative humidity data were obtained from the ERA5 reanalysis dataset, provided by the European Centre for Medium-Range Weather Forecasts (ECMWF)(ECMWF, 2020). The annual rainfall averages between 500 and 1,000 millimetres. Woodlands encompass 28.4% of the region, with the majority of farmlands located near villages (Nations, 2010).

2.2. Material

2.2.1. Sentinel-2 Data

Launched in June 2015, the Sentinel-2A and Sentinel-2B satellites have Multi-Spectral Instruments (MSI) that can collect data every five days across a 290-kilometer radius. Three 60-meter atmospheric bands, six 20-meter red-edge, near-infrared, and shortwave infrared bands, and four 10-meter visible and near-infrared bands make up the instruments' 13 spectral bands. For this investigation, Sentinel-2B MSI's Level-1C top-of-atmosphere reflectance data were utilized. Sentinel-2A MSI Level-2A land surface reflectance data, atmospherically corrected, were derived from ESA Copernicus imagery acquired in July between 2000 and 2024. (Isbaex and Coelho, 2021).

2.2.2. Landsat Datasets

For this study, we acquired Landsat images (OLI/TIRS C1 Level-1) and Landsat 7 ETM+ data from 2000 to 2024 from USGS's GloVis, selecting images with less than 10% cloud cover (USGS, 2017). Atmospheric correction was performed using the FLAASH algorithm in ENVI 5.3, and vegetation indices like NDVI, TWI, NDMI, and NBR were calculated for each Landsat image, mirroring the data processing of Sentinel-2(SUHET, 2015).

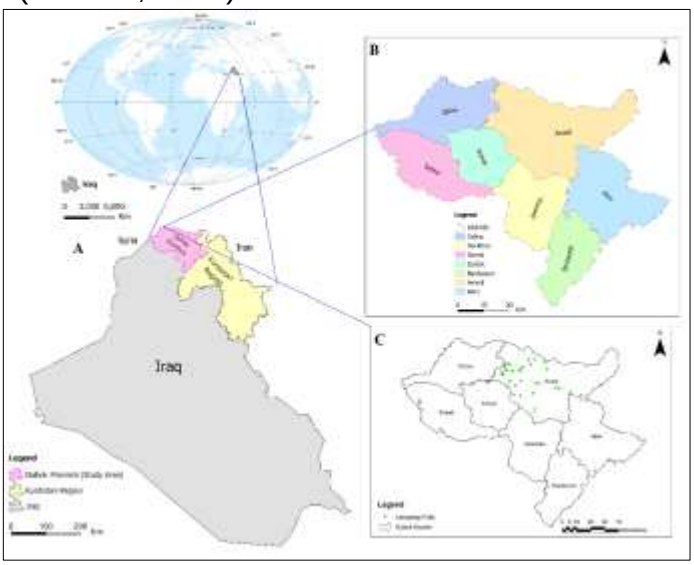

Figure 1: (A) Cartographic representation of Iraq, (B) Cartographic representation of the study area in the DU Government, (C) Distribution points of Validation Sampling.

2.3. Methodology

The methodology initiates in Figure 3, commencing with data acquisition, involving satellite imagery from Landsat 5 Thematic Mapper (TM), Landsat 7 Enhanced Thematic Mapper Plus (ETM+), Landsat 8 Operational Land Imager (OLI), and Sentinel 1 & 2, in conjunction with field measurements obtained through Google Earth. Thermal Infrared Sensor (TIRS) data is also harnessed for thermal infrared processing. These datasets serve as the fundamental inputs for subsequent analysis(Bohlmann and Koller, 2020; Niro et al., 2021; Roy et al., 2014). ML algorithms efficiently detect changes in forest cover by analyzing large data sets to find trends and patterns. Using models to identify and measure changes in forest land (FL) and non-forest land (non-FL) areas over time is the next step in the analysis of forest cover changes. According to Hansen et al. (2013), this offers information on trends in afforestation or deforestation within the study area.

2.3.1. Data Processing and Validation

During the data preprocessing phase, the satellite imagery undergoes multiple processes, including image resampling and atmospheric corrections to derive bottom-of-atmosphere (BOA) reflectance. Pan-sharpening is applied to Landsat data to enhance spatial resolution (Roy et al., 2014). Delineating the boundaries of the study area is followed by mosaicking and sub-setting to focus on the area of interest. We assessed vegetation dynamics using Landsat and Sentinel-2 imagery, widely used in environmental research. Following Congalton and Green (2009), we employed ground-truth validation to ensure satellite data accuracy. Satellite data validation for the Amedee native forest used field data from 32, 50x50 m plots Appendix Table A1, as reliable remote sensing requires it (Congalton and Green, 2019). We further strengthened our findings with cross-validation using field survey data, as detailed by (Kamusoko, 2022) .Preprocessing addressed cloud cover and atmospheric disturbances, crucial steps highlighted by (Liu et al., 2004).

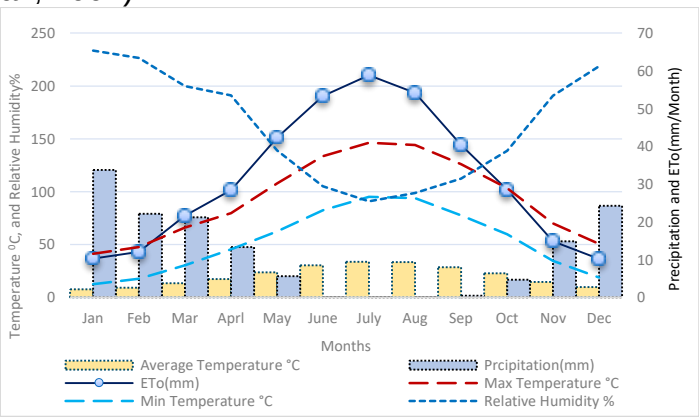

Figure 2: Monthly precipitation, relative humidity, actual evaporation, maximum, minimum, and mean temperature of DU Government for the period spanning from 1997 to 2023.

2.3.2. Scan Line Corrector(SLC) -off Gap Mitigation via Compositing and Sensor Fusion

The Google Earth Engine (GEE) was utilized to process Landsat 7 ETM+ imagery following the Scan Line Corrector (SLC) failure after May 31, 2003. Images were selected from the LANDSAT/LE07/C02/T1_L2 collection, filtered for <10% cloud cover, and preprocessed using the QA_PIXEL band and FMask to remove clouds and shadows(Roy et al., 2016; Zhu and Woodcock, 2012)To mitigate the effects of Landsat 7 SLC-off data gaps, a seasonal stack of cloud-free images was generated using Julian day filtering to ensure phenological consistency, with only valid (cloud- and gap-free) pixels retained via quality masks.

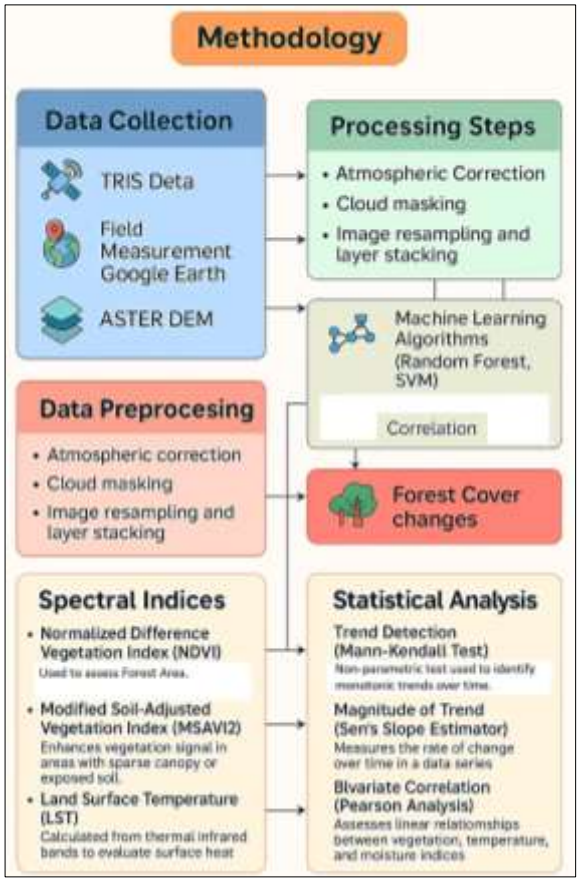

Figure 3: Flow diagram showing the methodology.

A pixel-wise median composite was then constructed using the GEE median () reducer to minimize outliers and preserve spectral integrity. In regions where data gaps remained, auxiliary imagery from Landsat 8 OLI and Sentinel-2 MSI was incorporated. These datasets were harmonized through linear regression-based reflectance normalization and resampled to 30 m resolution to ensure spatial and spectral compatibility(Roy et al., 2016).

2.3.3. Spectral Indices

2.3.3.1. Normalized Differences Vegetation Index (NDVI)

The NDVI index is calculated based on the reflectance of the red (Red) and the Near-Infrared (NIR) bands of the Landsat images, using formula 1, as follows:

$$\mathbf{NDVI} = \frac{\boldsymbol{NIR-Red}}{\boldsymbol{NIR+Red}} \quad \text{..... 1}$$

Theoretically, NDVI values ranged between −1.0 and +1.0. However, the typical range of the NDVI index from vegetation and other earth surface materials is between approximately −0.1 (NIR less than Red) for no vegetated surfaces and as high as 0.9 for dense vegetative cover. NDVI values increase with increasing green biomass, positive seasonal changes, and favorable factors (e.g., abundant precipitation) (Anyamba and Tucker, 2012; Aquino et al., 2018; Schmidt, 2017; Taufik et al., 2017).

2.3.3.2 The Modified Soil-Adjusted Vegetation Index (MSAVI2)

The second vegetation index included in this study, MSAVI2, is a revision of the modified soil-adjusted vegetation index (MSAVI2). This index is a refinement of SAVI that minimizes user error in setting the correction factor by more reliably and simply calculating a soil brightness correction factor (J Qi et al., 1994). The index also ranges from -1 to +1 and is calculated per-pixel according to the following formula (Jiaguo Qi et al., 1994).

$$MSAV12 = \frac{2\rho NIR+1-\sqrt{(2\rho NIR+1)^2-8*(\rho NIR-\rho RED)}}{2} \quad \text{... ...2}$$

Where ρ is the reflectance in the near-infrared (NIR) or red (RED) band.

2.3.3.3 Land Surfaces Temperature (LST)

The LST fraction images were produced using the Landsat thermal bands, bands 6 of the L5 TM, L7 ETM+, and bands 10–11 of L8 TIRS. Brightness temperature can be calculated using Planck's law (Dash et al., 2002). Using Top of the Atmosphere (TOA) radiances obtained from TIR sensors. Band 6 of TM/ETM+ and Band 10 of OLI images were utilized for retrieving the LST images (Sun et al., 2009). Equations used for converting digital numbers into land surface temperature in Landsat 8 are presented as follows:

Conversion of DN Digital Number to a Satellite Brightness Temperature

$$TB = \frac{K2}{\ln\left(\left(\frac{K1}{L\lambda}\right)+1\right)} \quad \text{.....3}$$

Where:

$K1$ = Band-specific thermal conversion constant (In watts/meter squared * ster * μm)

$K2$ = Band-specific thermal conversion constant (in kelvin)

Lλ is the spectral radiance at the sensor's aperture, measured in watts/(meter squared * ster * μm).

Calculation of the Land Surface Temperature in Kelvin

$$\boldsymbol{T = TB / [1 + (\lambda * TB / \rho) ln\varepsilon]} \quad \text{.....4}$$

Where:

λ = wavelength of emitted radiance

ρ = h * c/σ (1.438 × 10−2m·K)

h = Planck's constant (6.626 × 10−34 J·s)

σ = Boltzmann constant (1.38 × 10−23 J/K)

c = velocity of light (2.998 × 108 m/s)

ε = emissivity, which is given by the following: (Donglian Sun, 2007)

ε = 1.009 + 0.047 ln (NDVI)

Conversion from Kelvin to Celsius

$$\boldsymbol{Tc = T - 273.15} \quad \text{..... 5}$$

$\boldsymbol{T}$ = land surface temperature in Kelvin

$\boldsymbol{Tc}$ = land surface temperature in Celsius (Dash et al., 2002). The temperature transformation of the thermal infrared band into the value of ground temperature is done using the following equations for Landsat 5 and Landsat 7:

Convert DN to radiance = **0.05518*(i1) +1.2378**... 6

Convert radiance to Kelvin = **1260.56/log ((666.09/i1) +1)** ……..……7

Convert Kelvin to Celsius = **i1-273.15** …..…… 8

Whereas, i1 = the reflectance of the thermal infrared band. where L is value of radiance in thermal infrared; T is ground temperature (K); Q is digital record; K1 and K2 are calibration coefficients: K1=666.09 W/(m2 ster mm) and K2=1282.71 K; Lmin=0.1238 W/(m2 ster mm); and Lmax=1.500 W/(m2 ster mm).

Then the changes were compared among the five drought categories, and the one that showed the largest change compared to the other 4 categories was selected as the dominant one.

2.3.3.4. Normalized Difference Moisture Index (NDMI)

The Normalized Difference Moisture Index (NDMI) standardizes the various moisture response bands across the near-infrared (NIR) and shortwave infrared (SWIR) spectra (as per Equation (9)). The linear relationship between the NIR/SWIR ratio and leaf relative water content was initially identified by (Hunt and Rock, 1989). They computed the NDMI utilizing the following formula:

$$S = \sum_{i=1}^{n-1} \sum_{j=i+1}^{n} sign(\mathbf{Tj} - \mathbf{Ti}) \quad \text{..... 9}$$

$$\text{NDMI} = (\text{NIR} - \text{SWIR}) / (\text{NIR} + \text{SWIR}) \quad \text{..... 10}$$

Where NIR corresponds to the Near-Infrared spectrum and SWIR pertains to the Shortwave Infrared spectrum. The NDMI scale spans from -1 to 1, where values closer to 1 signify abundant moisture levels within vegetation, whereas values nearing -1 indicate a moisture deficiency.

2.3.4. Statistical Analysis

2.3.4.1. Trend Detection (Mann-Kendall Test)

Mann–Kendall tests are a statistical test widely used for trend analysis in time series of environmental data, hydrological data, and climatological time series. To detect monotonic trends, the nonparametric Mann-Kendall test is frequently used (Gilbert, 1987; Pohlert, 2016; Qutbudin et al., 2019). There are two advantages of using this test. First, it is a nonparametric test and does not require data to be normally distributed. Secondly, the test exhibits low sensitivity to sudden interruptions resulting from inhomogeneous time series (Corps and Lukas, 2005). The computational procedure for Mann–Kendall test considers the time series of n data points and Ti and Tj as two subsets of data where i = 1,2, 3…, n-1 and j = i+1, i+2, i+3, …, n. The data values are evaluated as an ordered time series. Each data value is compared to the subsequent data values. If a data value from a later time exceeds a data value from earlier times, the statistic S is increased. On the other hand, if the data value from a later time is lower than a data value sampled earlier, S is decremented. The net result of all such increments and decrements yields the final value of S (Atilgan et al., 2017; Gilbert, 1987; Pohlert, 2016). The Mann–Kendall S Statistic is computed as follows:

$$sign(\mathbf{Tj} - \mathbf{Ti}) = \begin{cases} \mathbf{1}\ if\ \mathbf{Tj} - \mathbf{Ti} > \mathbf{0} \\ \mathbf{0}\ if \mathbf{Tj} - \mathbf{Ti} = \mathbf{0} \\ -\mathbf{1}\ if\ \mathbf{Tj} - \mathbf{Ti} < \mathbf{0} \end{cases} \quad \text{.. 11}$$

Where Tj and Ti are the annual maximum daily values in years' j and i, j > i, respectively. If n < 10, the value of |S| is compared directly to the theoretical distribution of S derived by Mann and Kendall. The two-tailed test is used. At a certain probability level, H0 is rejected in favor of H1 if the absolute value of S equals or exceeds a specified value Sα/2, where Sα/2 is the smallest S which has a probability less than α/2 to appear in case of no trend. A positive (negative) value of S indicates an upward (downward) trend. For n ≥ 10, the statistic S is approximately normally distributed with the mean and variance as follows: E(S)=0, S (Atilgan et al., 2017; Gilbert, 1987; Pohlert, 2016). The variance (σ2) for the S-statistic is defined by the following:

$$\sigma^2 = \frac{n(n-1)(2n+5) - \sum t_i(i)(ti-1)(2ti+5)}{18} \quad \text{...12}$$

In which ti denotes the number of ties to extent i. The summation term in the numerator is used only if the data series contains tied values. The standard test statistic Zs is calculated as follows:

$$Z_s = \begin{cases} \frac{s-1}{\sigma}\ forS > 0 \\ 0\ for\ S = 0 \\ \frac{s+1}{\sigma} forS < 0 \end{cases} \quad \text{..... 13}$$

The test statistic Zs was used as a measure of the significance of the trend. For example, if -1.96 < Z < 1.96 = No trend, Z > 1.96 = Increase in trend, Z < -1.96 = Decrease in trend (Hamed, 2008; Kahya and Kalayci, 2004; Partal and Kahya, 2006).

2.3.4.2. The magnitude of Trend (Sen's slope)

The Sen's Slope estimator is a nonparametric, linear slope estimator that works most efficiently on monotonic data. Different linear regression is not significantly affected by gross data errors, outliers, or missing data. Sen's Slope

method was used to regulate the scale of the trend line. This test computes both the slope, i.e., the linear rate of change, and the intercept according to Sen's method. First, a set of linear slopes was calculated as follows:

$$dk = XJ - Xi/j - i \quad \text{…….…....…. 14}$$

For (**1 ≤ i< j ≤ n**), where d is the slope, X denotes the variable, n is the number of data, and i, j are indices. Sen's slope is then calculated as the median from all slopes:
b = Median dk. The intercepts are computed for each time step t as given by the following:
The intercepts are computed for each time step t as given by at

$$= Xt - b * t \quad \text{…….…..... 15}$$

In addition, the corresponding intercept is also the median of all intercepts. This function also computes the upper and lower confidence limits for sense slope (Pohlert, 2016).
Figure 3 visually outlines the study's methodology, from data acquisition and preprocessing to index calculation and results interpretation. It highlights remote sensing and geospatial analysis for assessing environmental changes.

2.3.4.3. Bivariate (Pearson) Correlation Analysis

A linear Correlation between observed and simulated variables was tested by the Pearson correlation coefficient, which ranges from −1 to +1, with p < 0.05 denoting significance at the 95% confidence level. The sign indicates the direction of the relationship while the absolute value indicates its strength; larger absolute values represent stronger positive or negative associations. (Field, 2024).

$$r = (n\sum xy - (\sum x)(\sum y)) / \text{sqrt}([n\sum x^2 - (\sum x)^2][n\sum y^2 - (\sum y)^2]) \quad \text{……..16}$$

where: r = Pearson Correlation Coefficient, n = number of pairs of observations, ∑xy = sum of products of the paired scores, ∑x = sum of the x scores, ∑y = sum of the y scores, ∑x² = sum of the squared x scores, ∑y² = sum of the squared y scores

2.3.4.4. ARIMA Modeling and Equation Explanation

ARIMA (Auto Regressive Integrated Moving Average) is a widely used statistical method for time series forecasting (Seymour et al., 1997). The ARIMA model is denoted as ARIMA (p, d, q), where p represents the number of lagged observations in the AR term, d indicates the number of times differencing is applied to make the series stationary, and q specifies the number of lagged forecast errors in the MA term. Before calculating the Variance Inflation Factor (VIF) for each predictor: $VIF_i = 1 / (1 - R_i^2)$, where R_i^2 is the R-squared from regressing the i-th predictor against all other predictors. A VIF exceeding 5 indicates multicollinearity, which can distort estimates; redundant predictors should be removed or combined (O'Brien, 2007), where VIF is calculated from the coefficient of determination ($Ri2$) obtained by regressing the i-th predictor on all others. Following multicollinearity remediation, the Auto Regressive Integrated Moving Average (ARIMA) approach can be used for time series forecasting (Seymour et al., 1997). An ARIMA(p,d,q) model is defined by three parameters: p, the number of autoregressive (AR) terms (lagged values of Y); d, the order of differencing required for stationarity; and q, the number of moving average (MA) terms (lagged forecast errors). The general ARIMA(p,d,q) equation is:

$$Yt = c + \Sigma pi{=}1\ \phi i\ Yt{-}i + \Sigma qj{=}1\ \theta j\ \varepsilon t{-}j + \varepsilon t, \quad \text{…17}$$

where Yt is the time series value at time t, c is a constant, ϕi are the AR coefficients, θj are the MA coefficients, and εt is white noise. When differencing (d) is required for stationarity, the ARIMA model is applied to the differenced series (Hyndman and Athanasopoulos, 2018). Addressing multicollinearity and confirming stationarity improve the reliability of ARIMA parameter estimates and forecasts. In this study, all results were evaluated at a 95% confidence level. We assessed the model's technical validity and practical implications through model specification, parameter estimates, diagnostic

statistics, residual analysis, and forecasting performance. An ARIMA (1,0,0) model with no seasonal components (P=0, D=0, Q=0, s=0) was selected, estimated via likelihood-based optimization with a convergence threshold of 0.00001 and a maximum of 500 iterations. 95% confidence intervals were reported for robust statistical inference. This basic autoregressive specification, suitable for a series exhibiting first-order persistence under stationarity, omits differencing or moving-average terms.

Overall, the ARIMA (1,0,0) model demonstrates a strong fit, capturing key autocorrelation structures with low residual errors and accurate near-term predictions.

3. Results and Discussion

3.1. Amedi District Forest Cover Change Analysis Using NDVI and MSAVI2, 2000–2024.

Figure 4 and Tables 1 and 2 present an analysis of (FL)trends in the Amidi region using the NDVI and MSAVI2 indices. The percentage of forest land decreased significantly from 90.3% (2505.3 km^2) in 2000–2001 to 73.3% (2032.2 km^2) in 2023–2024, according to the NDVI data in Table 2. Comparable declines are also shown in the MSAVI2 data, which went from 86.3% (2393.3 km^2) to 74.3% (2062.3 km^2) during the same period.

The ARIMA (1,0,0) model was applied to the time series, with parameters optimized using the likelihood method. The constant term was estimated at 2011.500, with a 95% confidence interval of [1990.093, 2032.907], while the autoregressive coefficient AR (1) was 0.996, with confidence intervals of [0.985, 1.007] (Hessian) and [0.960, 1.032] (asymptotic). These narrow intervals and the AR coefficient close to 1 indicate a strong temporal dependence in the series. The absence of differencing (d = 0) suggests that the series is stationary, implying that the Augmented Dickey-Fuller (ADF) test would reject the null hypothesis of a unit root, supporting the use of ARIMA without differencing. The model demonstrated a good fit, with a Root Mean Square Error (RMSE) of 1.000, a Mean Absolute Percentage Error (MAPE) of 0.050, and an Akaike Information Criterion (AIC) of 76.920, indicating high predictive accuracy and model reliability.

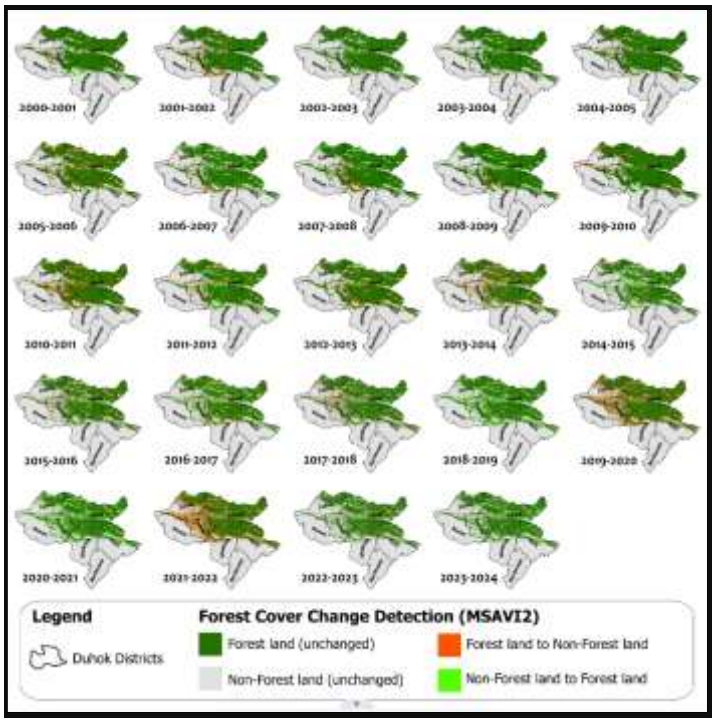

Figure 4: Spatiotemporal Fluctuation of MSAVI2 in Amadi District (2000–2021).

These statistics underscore the growing pressures of deforestation by showing a notable decline in wooded areas. Additionally, the proportion of wooded area turning into non-forest land increased steadily. Deforestation has risen from 2.4% (66.5 km^2) in 2000–2001 to 4.4% (121.6 km^2) in 2023–2024, according to the NDVI classification. This points to increased land conversion and a notable rise in deforestation from 2012–2015 to 2020–2024. NDVI, MSAVI2, and Land Surface Temperature (LST) data were used to conduct a time series study of (FL) changes in Amedi District from 2000 to 2024, and the results show some noteworthy patterns. The NDVI decreased from 90.3% (2505.3 km2) in 2000–2001 to 73.3% (2032.2 km^2) in 2023–2024, indicating a steady decline in forest areas. These findings are consistent with regional studies. In northern Iraq and western Iran, NDVI-based assessments have documented similar declines due to prolonged droughts, overgrazing, and poor forest governance(Gaznayee et al., 2022; Kim et al., 2024).Turkey's Eastern Anatolia and Taurus Mountains have experienced forest degradation driven by urban expansion, fire, and unsustainable logging practices (Gholamnia et al., 2019; Kim et al., 2024)..In Lebanon, areas like

Mount Lebanon and Bekaa have shown NDVI reductions linked to civil conflict, wildfires, and informal land use changes. (Elsa Sattout et al., 2005). These cross-national patterns suggest that forest degradation in Amedi is not isolated but part of a broader phenomenon tied to both environmental stress (e.g., drought and warming) and socio-political instability.

Table 1: Time series changes in MSAVI2 for Amedi District from 2000 to 2024.

MSAVI2	Forest Land		(FL)to Non-(FL)		Non-(FL)to (FL)		Non-(FL)	
Years	Area (km²)	%	Area (km²)	%	Area (km²)	%	Area (km²)	%
2000-2001	2393.3	86.3	76.5	2.8	56.4	2.0	247.6	8.9
2001-2002	2363.9	85.2	85.7	3.1	41.6	1.5	282.4	10.2
2002-2003	2379.2	85.8	26.3	0.9	48.2	1.7	319.9	11.5
2003-2004	2412.9	87.0	14.5	0.5	67.7	2.4	278.5	10.0
2004-2005	2439.6	87.9	41.0	1.5	47.8	1.7	245.3	8.8
2005-2006	2167.2	78.1	320.2	11.5	43.0	1.6	243.2	8.8
2006-2007	2167.2	78.1	43.0	1.6	251.5	9.1	312.0	11.2
2007-2008	2394.1	86.3	24.6	0.9	211.1	7.6	143.9	5.2
2008-2009	2395.9	86.4	13.3	0.5	209.3	7.5	155.2	5.6
2009-2010	2533.2	91.3	72.0	2.6	35.4	1.3	133.0	4.8
2010-2011	2261.3	81.5	307.2	11.1	40.1	1.4	165.0	5.9
2011-2012	2157.1	77.8	144.3	5.2	242.8	8.8	229.4	8.3
2012-2013	2189.1	78.9	210.8	7.6	134.2	4.8	239.6	8.6
2013-2014	2007.3	72.4	316.0	11.4	8.3	0.3	442.1	15.9
2014-2015	1962.7	70.8	52.9	1.9	256.3	9.2	501.8	18.1
2015-2016	2037.0	73.4	182.0	6.6	68.7	2.5	486.0	17.5
2016-2017	1979.4	71.4	126.3	4.6	260.8	9.4	407.2	14.7
2017-2018	2126.2	76.6	114.0	4.1	48.1	1.7	485.4	17.5
2018-2019	2164.8	78.0	9.4	0.3	324.4	11.7	275.0	9.9
2019-2020	2125.4	76.6	363.9	13.1	3.5	0.1	280.9	10.1
2020-2021	2113.7	76.2	15.2	0.5	365.7	13.2	279.0	10.1
2021-2022	2091.9	75.4	387.5	14.0	12.9	0.5	281.3	10.1
2022-2023	2017.4	72.7	87.4	3.2	74.8	2.7	594.0	21.4
2023-2024	2062.3	74.3	29.9	1.1	193.7	7.0	487.8	17.6

Table 1 and Figure 4's MSAVI2 statistics demonstrate a decrease during the same time period, going from 86.3% (2393.3 km^2) to 74.3% (2062.3 km^2). This ongoing decline in forest cover suggests a more significant degree of deforestation resulting from environmental degradation, agricultural expansion, and urbanization. The NDVI data depict a rise from 2.4% (66.5 km²) in 2000–2001 to 4.4% (121.6 km²) by 2023–2024. The most substantial increases were observed during the periods of 2013–2015 and 2020–2024, indicating intensified alterations in land usage and potential climatic impacts like drought. In contrast, the rates of reforestation (transitions from non-forest to forested areas) remained relatively meager over the years, making minimal contributions to the overall restoration of forested regions(Huebner et al., 2022a). The examination of non-forest areas reveals an escalation from 5.8% (160.8 km²) in 2000–2001 to 19.7% (546.6 km²) in 2023–2024. This expansion aligns with a decrease in forested regions and signifies significant modifications in land use, likely stemming from human interventions and natural deterioration(Abdalkarim et al., 2023).

Table 2: Time series changes in NDVI for Amedi District from 2000 to 2024.

NDVI	Forest Land		(FL) to Non-(FL)		Non-(FL) to (FL)		Non-(FL)	
Years	Area (km²)	%	Area (km²)	%	Area (km²)	%	Area (km²)	%
2000-2001	2505.3	90.3	66.5	2.4	41.1	1.5	160.8	5.8
2001-2002	2485.5	89.6	60.9	2.2	51.3	1.8	175.9	6.3
2002-2003	2353.1	84.8	183.0	6.6	93.5	3.4	144.0	5.2
2003-2004	2428.2	87.5	80.0	2.9	121.5	4.4	144.0	5.2
2004-2005	2560.2	92.3	46.1	1.7	49.8	1.8	117.6	4.2
2005-2006	2565.8	92.5	44.2	1.6	35.2	1.3	128.4	4.6
2006-2007	2488.9	89.7	112.0	4.0	45.6	1.6	127.1	4.6
2007-2008	2437.2	87.9	97.3	3.5	101.5	3.7	137.7	5.0
2008-2009	2516.5	90.7	22.2	0.8	129.0	4.7	106.0	3.8
2009-2010	2500.4	90.1	145.0	5.2	32.3	1.2	95.9	3.5
2010-2011	2512.5	90.6	20.2	0.7	106.6	3.8	134.3	4.8
2011-2012	2524.1	91.0	95.0	3.4	54.5	2.0	100.0	3.6
2012-2013	2432.7	87.7	145.9	5.3	58.4	2.1	136.6	4.9
2013-2014	2355.6	84.9	135.5	4.9	28.9	1.0	253.6	9.1
2014-2015	2311.6	83.3	72.9	2.6	127.2	4.6	261.9	9.4
2015-2016	2294.3	82.7	144.5	5.2	64.3	2.3	270.6	9.8
2016-2017	2159.3	77.8	199.0	7.2	94.6	3.4	321.0	11.6
2017-2018	2187.4	78.9	39.2	1.4	168.8	6.1	378.4	13.6
2018-2019	2224.1	80.2	132.1	4.8	52.8	1.9	364.7	13.1
2019-2020	2141.9	77.2	135.0	4.9	47.5	1.7	449.3	16.2
2020-2021	2092.8	75.4	96.6	3.5	114.1	4.1	470.2	17.0
2021-2022	2131.7	76.8	75.1	2.7	131.2	4.7	435.7	15.7
2022-2023	2110.6	76.1	152.3	5.5	43.2	1.6	467.6	16.9
2023-2024	2032.2	73.3	121.6	4.4	73.3	2.6	546.6	19.7

3.2. LST Changes in Amedi District, 2000–2024.

The LST data presented in Table 3 and Figure 5 depict the analysis of (LST) categories for Amedi District from 2000 to 2024 revealing a pronounced shift from cooler to warmer temperature ranges. In 2000–2001, Very Low LST (<35°C) covered around 849 km², making it one of the largest categories at the start of the analysis. Over time, this category consistently declined, dropping to approximately 520 km² by 2023–2024. A similar trend is observed for the Low LST class (35–40°C), which started at around 1062 km² and decreased to about 790 km² by the end of the study period. Since 2000–2001, the "Moderate" LST category (40–45°C) has gradually grown from around 732 km² to over 800 km² in 2023–2024. This increasing shift sees the district's ongoing adaptation to increased temperatures. In recent years, the High LST class (45–50°C) has grown from about 263 km² to values above 300 km². Of particular note is the increase in the Extreme LST class (>50°C). In the first few years (2000–2001), no area experienced surface temperatures above 50°C. However, around 2002–2003, small areas of intense heat began to emerge, ranging in size from roughly 1 km² to 26

km² in different years. Although the total coverage of these Extreme zones is still relatively small, their presence highlights the intensity of warming in certain concentrated portions of the district.

Table 3: Time series changes in LST for Amedi District from 2000 to 2024.

LST	Very low ≤35		Low <35-40>		Moderate <40-45>		High <45-50>		Extreme ≥50	
Years	Area (km²)	%	Area (km²)	%	Area (km²)	%	Area (km²)	%	Area (km²)	%
2000-2001	849.3	30.6	1042.2	37.6	732.3	26.4	146.4	5.3	3.4	0.1
2001-2002	406.1	14.6	938.4	33.8	964.6	34.8	436.1	15.7	28.4	1.0
2002-2003	811.6	29.3	1018.2	36.7	759.3	27.4	184.1	6.6	0.4	0.0
2003-2004	1125.9	40.6	1056.6	38.1	569.3	20.5	21.9	0.8	0.0	0.0
2004-2005	650.6	23.5	997.2	35.9	745.6	26.9	377.9	13.6	2.4	0.1
2005-2006	660.2	23.8	937.9	33.8	855.7	30.8	316.1	11.4	3.7	0.1
2006-2007	462.5	16.7	975.8	35.2	884.3	31.9	418.5	15.1	32.5	1.2
2007-2008	565.8	20.4	935.3	33.7	840.5	30.3	401.5	14.5	30.6	1.1
2008-2009	550.6	19.8	805.3	29.0	911.5	32.9	453.0	16.3	53.3	1.9
2009-2010	863.8	31.1	1309.9	47.2	575.7	20.8	23.8	0.9	0.5	0.0
2010-2011	581.3	21.0	832.6	30.0	1063.5	38.3	294.0	10.6	2.2	0.1
2011-2012	950.1	34.3	542.7	19.6	1087.9	39.2	192.8	7.0	0.1	0.0
2012-2013	391.9	14.1	825.5	29.8	1194.0	43.0	357.7	12.9	4.5	0.2
2013-2014	783.5	28.2	1075.6	38.8	703.7	25.4	207.7	7.5	3.1	0.1
2014-2015	250.5	9.0	804.0	29.0	992.0	35.8	623.4	22.5	103.8	3.7
2015-2016	647.0	23.3	1064.1	38.4	811.1	29.2	249.1	9.0	2.3	0.1
2016-2017	577.0	20.8	1211.0	43.7	837.8	30.2	147.9	5.3	0.0	0.0
2017-2018	196.2	7.1	784.3	28.3	1175.4	42.4	606.2	21.9	11.5	0.4
2018-2019	459.5	16.6	1013.0	36.5	862.0	31.1	395.7	14.3	43.5	1.6
2019-2020	502.7	18.1	1008.1	36.3	908.2	32.7	327.3	11.8	27.4	1.0
2020-2021	235.0	8.5	915.6	33.0	1047.3	37.8	493.7	17.8	82.0	3.0
2021-2022	248.7	9.0	778.7	28.1	1002.9	36.2	723.8	26.1	19.5	0.7
2022-2023	155.5	5.6	645.8	23.3	1021.8	36.8	873.0	31.5	77.5	2.8
2023-2024	520.3	18.8	989.3	35.7	896.1	32.3	365.6	13.2	2.4	0.1

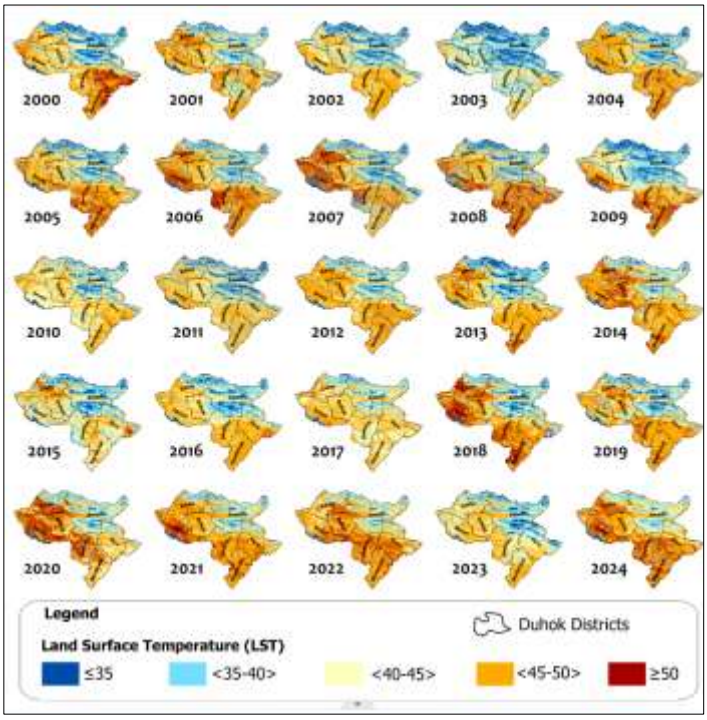

Figure 5: Spatiotemporal Fluctuation of LST in Amedi District (2000–2021).

These results are consistent with more general trends in climate change that have been seen locally and globally. Rising average temperatures associated with higher quantities of greenhouse gases and changing atmospheric dynamics are compatible with the expansion of warmer classes and the decline of cooler LST categories (Mohammad et al., 2025). Local variables that affect the land's surface characteristics, like urbanization, deforestation, and changes in farming techniques, might intensify these trends significantly.

3.3. NDMI Changes in Amedi District, 2000–2024

Table 4 displays the NDMI data for Amedi District. The time-series study of the (NDMI) for Amedi District from 2000 to 2024 divides the district into five categories. At the start of the study period (2000-2001), the Very Dry class was virtually absent (0.0 km²), whereas Moist and Very Moist conditions covered considerable areas of the territory (about 1367.5 km² and 139.0 km², respectively). In contrast, the Moderate class covered around 1089.9 km². This initial distribution indicates that Amedi District began the early 2000s with slightly even moisture conditions, biased toward the Moderate and Moist categories.

Table 4: Time series changes in NDMI for Amedi District from 2000 to 2024.

NDMI	Very dry		Dry		Moderate		Moist		Very moist	
Years	Area (km²)	%	Area (km²)	%	Area (km²)	Area (km²)	%	Area (km²)	%	Area (km²)
2000-2001	0.0	0.0	171.0	6.2	850.0	30.6	1367.5	49.3	385.2	13.9
2001-2002	0.0	0.0	342.5	12.3	1089.9	39.3	1033.6	37.3	307.6	11.1
2002-2003	0.0	0.0	272.9	9.8	955.2	34.4	1171.0	42.2	374.6	13.5
2003-2004	0.2	0.0	272.7	9.8	1363.7	49.2	892.7	32.2	244.3	8.8
2004-2005	0.4	0.0	281.6	10.2	1108.6	40.0	1108.3	40.0	274.7	9.9
2005-2006	0.5	0.0	286.9	10.3	1019.8	36.8	1151.5	41.5	314.9	11.4
2006-2007	16.1	0.6	391.1	14.1	1467.0	52.9	742.7	26.8	156.7	5.6
2007-2008	105.0	3.8	602.9	21.7	1031.5	37.2	842.1	30.4	192.2	6.9
2008-2009	251.1	9.1	713.7	25.7	992.0	35.8	705.7	25.4	111.1	4.0
2009-2010	70.6	2.5	465.2	16.8	1039.1	37.5	925.6	33.4	273.2	9.8
2010-2011	39.1	1.4	353.8	12.8	1037.2	37.4	1065.6	38.4	278.0	10.0
2011-2012	0.0	0.0	107.2	3.9	785.5	28.3	1254.3	45.2	626.6	22.6
2012-2013	168.7	6.1	701.7	25.3	1148.1	41.4	664.5	24.0	90.7	3.3
2013-2014	92.7	3.3	401.3	14.5	864.0	31.1	963.5	34.7	452.0	16.3
2014-2015	255.0	9.2	591.5	21.3	865.2	31.2	786.7	28.4	275.2	9.9
2015-2016	115.3	4.2	488.1	17.6	899.5	32.4	935.9	33.7	334.7	12.1
2016-2017	134.5	4.9	501.9	18.1	881.7	31.8	915.8	33.0	339.6	12.2
2017-2018	71.7	2.6	435.1	15.7	1055.4	38.0	959.1	34.6	252.4	9.1
2018-2019	181.0	6.5	577.0	20.8	989.0	35.7	767.3	27.7	259.4	9.4
2019-2020	43.1	1.6	408.5	14.7	957.6	34.5	969.1	34.9	395.3	14.3
2020-2021	172.1	6.2	567.8	20.5	966.4	34.8	819.0	29.5	248.3	9.0
2021-2022	351.4	12.7	742.9	26.8	880.4	31.7	635.2	22.9	163.8	5.9
2022-2023	127.7	4.6	506.1	18.2	1104.8	39.8	831.9	30.0	203.1	7.3
2023-2024	224.2	8.1	630.9	22.7	967.0	34.9	741.9	26.7	209.6	7.6

2001–2002, there was a noticeable appearance of Very Dry conditions (171.0 km²), even as Dry remained at 0.0 km². Meanwhile, Moist areas slightly increased to around 1390.2 km², and Very Moist rose to 185.3 km², indicating that extreme dryness was localized while much of the district remained sufficiently moist. However, the subsequent years (2002–2003, 2003–2004,

and so on) exhibit more frequent fluctuations. Over the long term, the data show a gradual increase in Dry and occasional Very Dry coverage from the mid-2000s onward, though these categories fluctuate year by year. Concurrently, the Moist" and Very Moist classes vary substantially, with some years (e.g., 2010–2011) showing significant Moist area, while other periods (such as 2012–2013) see reductions in these wetter categories.

By 2023–2024, the Very Moist class remains present but shows indications of decline compared to the early 2000s, suggesting an overall shift toward drier conditions, at least in certain parts of the district. These findings point to notable variability in moisture conditions within Amedi District over the 24 years. Several factors likely contribute to this dynamic, including interannual changes in precipitation, shifts in temperature regimes, and land use transformations (such as deforestation, agricultural expansion)(Huebner et al., 2022b; Zaki et al., 2023).

3.4. The Mann-Kendall trend based on NDVI

The NDVI–Forest Land time series from 2000 to 2024 exhibits both periods of increase and decrease, reflecting dynamic changes in forest cover over time. In the early 2000s, the series shows a modest increase in NDVI values, which may indicate improvements in vegetation density or reforestation efforts during that time. However, starting in the mid to late 2000s, a clear downward trend emerges, with several consecutive years showing declining NDVI values. The fitted ARIMA (1,0,0) model captures these fluctuations effectively, smoothing short-term variability while preserving the broader trend. The forecast from 2025 to 2035 projects a continuation of this general decline, though short-term fluctuations remain possible. The increasing width of the 95% confidence intervals in the forecast reflects rising uncertainty, especially given the near-unit-root behavior of the AR (1) coefficient. The analysis depicted in Figure 6 delineate the temporal dynamics of vegetation cover throughout the study area from 2000 to 2024, revealing a statistically significant decline in forested regions. The computed Kendall's tau value of –0.638, accompanied by a highly significant p-value (< 0.0001), decisively rejects the null hypothesis of no trend, thereby affirming a consistent and statistically robust decline in vegetation over the 24 years. The Sen's slope estimator, which quantifies the magnitude of this trend, was determined to be –22.379 km² per year, with a 95% confidence interval spanning from –24.068 to –21.629 km²/year. This indicates that, on average, the study area has experienced a loss of approximately 22.4 km² of vegetated land annually, underscoring an alarming rate of forest degradation.

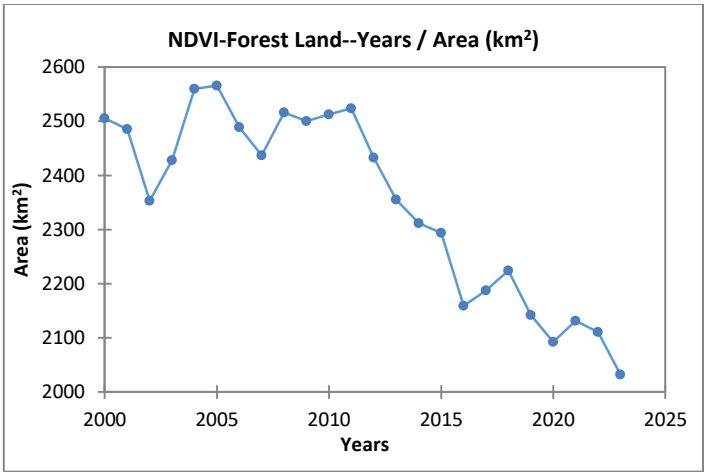

Figure 6: Trend of NDVI-Derived (FL)Area in Amedi District (2000–2024).

The strength of the slope, coupled with the narrow confidence interval, instills a high degree of confidence in the stability of this estimate. Consequently, the loss of vegetation is more reasonably attributed to persistent anthropogenic pressures and environmental changes rather than cyclical climatic or phenological patterns. These findings align with observed trends of deforestation, land conversion, and potential climate-induced stressors within the region (Mustafa, 2020; Habeeb and Mustafa, 2025). An ARIMA (1,0,0) model effectively captured and projected forest NDVI values from 2000 to 2024, forecasting up to 2035. The model, estimated via likelihood optimization with rapid convergence, demonstrated a strong fit, with RMSE and MSE around 1.0 and an MAPE of 5%. AIC (76.920) and SBC (79.276) values supported model parsimony.

A white noise variance of 0.999 indicated minimal residual autocorrelation. The AR (1) coefficient of 0.996 (95% CI: 0.985-1.007), along with a constant of 2011.500, suggests high NDVI persistence, with current forest conditions heavily influenced by previous years. While close to non-stationarity, the coefficient remained below 1.0, implying weak stationarity and warranting cautious interpretation and regular monitoring due to the potential for prolonged deviations from external shocks (Table A2). A 20-step-ahead forecast (2025-2035) revealed increasing uncertainty, with widening prediction intervals reflecting the near-unit AR (1) coefficient and the amplification of minor disturbances. This highlights the need for regular data updates and model recalibration for accurate long-term environmental monitoring.

3.5. The Mann-Kendall trend-NDMI

The Mann-Kendall trend analysis depicted in Figure 7 for the NDMI (Very Dry) region (km²) reveals a Kendall's tau coefficient of 0.594 and an exceptionally significant p-value (< 0.0001). Given that the p-value falls below the significance threshold of 0.05, we reject the null hypothesis (absence of trend) in favor of the alternative hypothesis, indicating a statistically noteworthy upward trend. The Sen's slope estimate stands at 8.92 km² per unit time, supported by a confidence interval spanning from 8.089 to 9.574 km², further confirming the presence of a consistent rising trend in very dry areas. In contrast, the Seasonal Mann-Kendall test (Period = 12) shows tau = 0.667, p = 0.256 > 0.05. Fail to reject the null hypothesis, no significant seasonal trend. Sen's slope of 124.624 suggests seasonal fluctuation, but lacks statistical significance, likely random variations.

The results show an increasing trend in very dry areas over time. Mann-Kendall test confirms an upward trajectory, indicating expansion of very dry conditions. Sen's slope of 8.92 km² per time unit highlights the persistent increase.

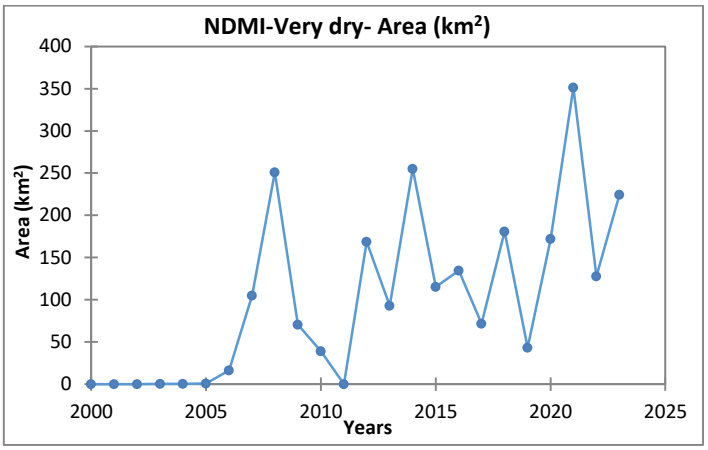

Figure 7: Trend of NDMI-Very Dry-Derived (FL)Area in Amedi District (2000–2024).

3.6. The Mann-Kendall trend test for-NDMI DRY

The Mann-Kendall trend examination illustrated in Figure 8 for the area (km²) reveals a Kendall's tau coefficient of 0.471 and a p-value of 0.001. Given that the p-value falls below the 0.05 threshold of significance, the null hypothesis (indicating no trend) is dismissed, thereby confirming the existence of a statistically noteworthy upward trend. The Sen's slope approximation stands at 14.157 km² per unit time, with a confidence interval spanning from 12.883 to 15.887 km², denoting a consistent expansion in area over time. The likelihood of erroneously rejecting the null hypothesis is exceedingly low (below 0.10%), further affirming the credibility of this trend. Conversely, the Seasonal Mann-Kendall test (Period = 12) shows Kendall's tau of 0.667 and a p-value of 0.256, exceeding the 0.05 threshold. Results show an upward trend in area over time, suggesting expansion or an increase in the phenomenon. Positive Kendall's tau and significant Sen's slope confirm the trend is consistent. The Mann–Kendall test analysis reveals a statistically significant positive trend in the Very Dry class values of the NDMI over the 24 years. The computed Kendall's tau coefficient of 0.471 and a p-value of 0.001 indicate a consistent and strong upward trend, suggesting a substantial and statistically robust shift in the extent of very dry areas. Furthermore, the Sen's slope estimate of 14.157 km² per year confirms a gradual yet steady increase in land area classified under Very Dry vegetation stress conditions. The 95% confidence interval for the Sen's slope, ranging

from 12.883 to 15.887 km²/year, reinforces the reliability and precision of this increasing trend. These findings are consistent with Iraq and Syria, where long-term drought patterns have intensified since the early 2000s due to climate variability and anthropogenic stressors, including deforestation and agricultural mismanagement. Math bout et al (2025) observed significant decreases in vegetation indices in northern Syria, coinciding with the onset of the 2006–2010 drought, which contributed to widespread agricultural collapse(Mathbout et al., 2025). Similarly, in northeastern Iraq, Al-Mustansiriyah et al. (2020) reported a progressive increase in land degradation and dry vegetation cover using NDVI and NDMI indices, especially in areas affected by conflict and population displacement(Hassan et al., 2020).

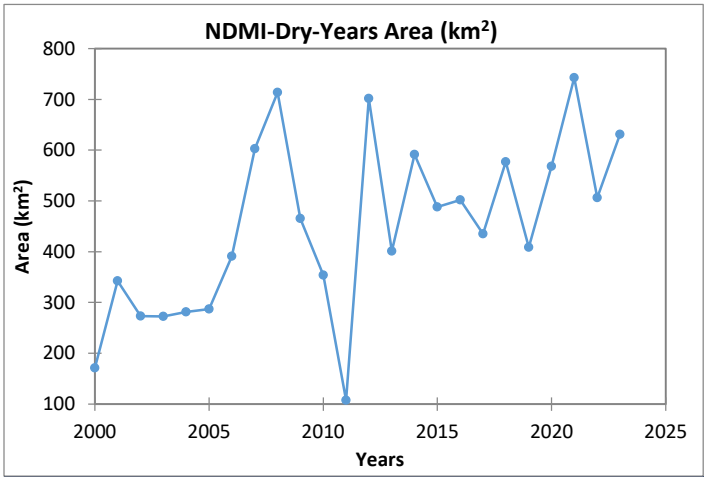

Figure 8: Trend of NDMI- Dry-Derived (FL)Area in Amedi District (2000–2024).

In contrast, Turkey and Iran, while also experiencing long-term climatic drying, have shown more spatial variability. In western and central Turkey, studies by Ozturk et al. (2017) indicated both declining and improving vegetation trends depending on local conservation policies and water availability(Ozturk et al., 2017). In Iran, the Zagros region has seen notable declines in forest cover and soil moisture, consistent with our finding of expanding very dry vegetation classes(Ghahraman and Sepaskhah, 2004), though mitigation through watershed andrangeland rehabilitation programs has shown some localized improvements. Lebanon, with its relatively humid microclimates, presents a contrasting case. While studies El Moujabber et al. (2021) have reported increasing dryness in eastern inland areas, coastal and highland zones have remained relatively stable due to better rainfall retention and forest protection programs(El Chami and El Moujabber, 2024). However, regions near the Syrian border have also seen stress linked to refugee influx and land use changes.

3.7. The Mann-Kendall trend test-MSAVI2

The Mann-Kendall trend analysis illustrated in Figure 9 for MSAVI2-(FL) (km²) reveals a Kendall's tau coefficient of -0.522 alongside a p-value of 0.000, falling below the threshold of 0.05, denoting statistical significance. Consequently, the null hypothesis, suggesting no discernible trend, is refuted in support of the alternative hypothesis, indicating a statistically notable negative trend. The Sen's slope estimate stands at -16.52 km² per unit time, accompanied by a confidence interval ranging from -17.141 to -15.153 km², affirming a consistent diminishing pattern in (FL) area over time. The probability of wrongly rejecting the null hypothesis is <0.02%, indicating high confidence. Results show a decreasing trend in MSAVI2-Forest Land, with significant forest loss. Negative Kendall's tau and Sen's slope confirm a consistent decline. An estimated decline of 16.52 km² per time unit points to deforestation. The lack of a seasonal trend suggests that the decline is not tied to seasons.

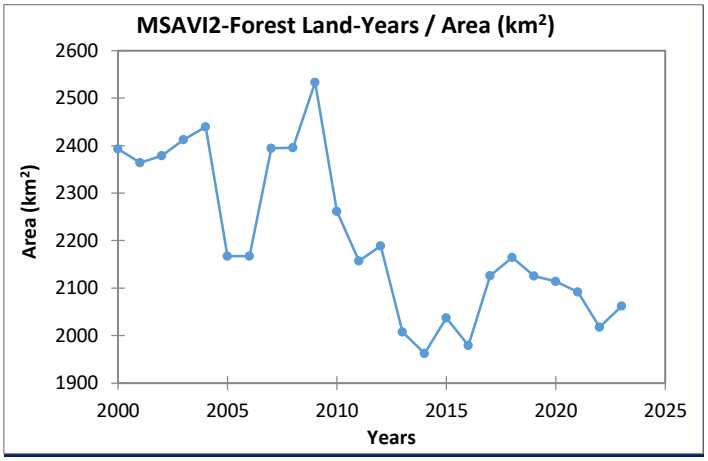

Figure 9: Trend of MSAVI2-Derived (FL)Area in Amedi District (2000–2024).

3.8. The Mann-Kendall trend test -LST

The Mann-Kendall trend analysis displayed

in Figure 10 for the LST-High (45-50°C) region (km²) reveals a Kendall's tau coefficient of 0.312 and a p-value of 0.034. Given that the p-value falls below the predetermined significance threshold of 0.05, we can confidently reject the null hypothesis (suggesting no trend) in favor of the alternative hypothesis, indicating a statistically significant upward trajectory. The Sen's slope estimate stands at 14.662 km² per unit time, accompanied by a confidence interval spanning from 13.808 to 17.192 km², thereby affirming a consistent escalation in highland surface temperature (LST) regions. The probability of erroneously dismissing the null hypothesis remains minimal, standing at less than 3.43%.

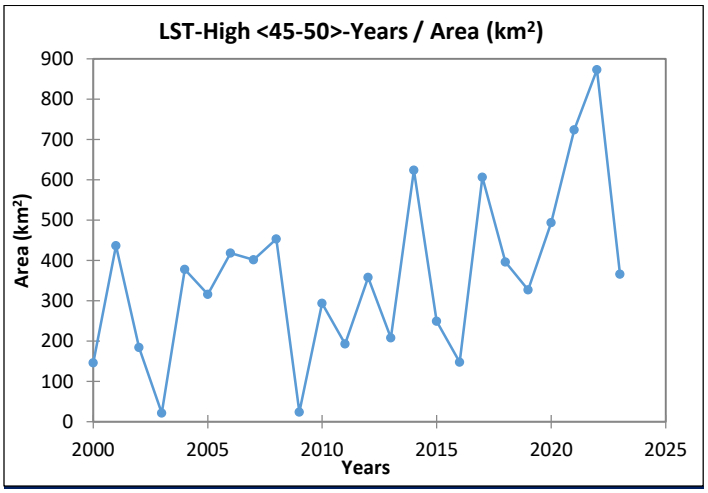

Figure 10: Trend of LST-High <45-50>-Derived (FL)Area in Amedi District (2000–2024).

The results show a significant increase in land surface temperature areas over time. Positive Kendall's tau and Sen's slope confirm this trend is not random, with high-temperature areas consistently expanding. The increase could be linked to urbanization, deforestation, climate change, or land-use changes. Sen's slope of 14.662 km² per time unit highlights the severity, indicating a need for further investigation into causes and mitigation strategies.

3.9. The Correlation matrix

Table 5 presents a Pearson correlation matrix illustrating the relationships among vegetation indices (NDVI and MSAVI2), Land Surface Temperature in the 45–50°C range (LST-High), NDMI for dry conditions (NDMI-Dry), and forest versus non-(FL)classifications in Amedi District. Several statistically significant correlations ($p < 0.05$) stand out. For instance, NDVI-(FL) is negatively correlated with LST-High (<45–50°C) ($r = –0.440$) and NDMI-Dry ($r = –0.431$), indicating that higher forest-based NDVI values are generally associated with lower high-range temperatures and lower dryness. Meanwhile, a strong positive correlation exists between NDVI-(FL) and MSAVI2-(FL) ($r = 0.656$), suggesting that these two vegetation indices capture similar patterns of forest cover and health. The matrix also reveals that LST-High (<45–50°C) is positively correlated with NDMI-Dry ($r = 0.513$), implying that areas experiencing higher land surface temperatures are more prone to dryness. In contrast, MSAVI2-(FL) has a moderate negative relationship with NDMI-Dry ($r = –0.501$), underscoring that higher FL cover (as measured by MSAVI2) tends to coincide with reduced dryness. Additionally, NDVI-(FL) shows a negative correlation ($r = –0.433$) with NDVI-F to Non-FL (NDVI for non-forest areas), suggesting that a strong vegetation signal in forested regions may coincide with lower NDVI readings in Non-FL regions within the same landscape.

Table 5: Pearson Correlation Matrix Relating Vegetation Indices (NDVI, MSAVI2), (LST), NDMI, and Forest land (FL)/Non-Forest land(Non-FL).

Variables	NDVI-FL	LST-High <45-50>	MSAVI2-FL	NDMI-Dry	MSAVI2- FL to Non-FL	NDVI-FL to Non-FL
NDVI- FL	1	**-0.440**	**0.656**	**-0.494**	-0.055	**-0.433**
LST-High <45-50>	**-0.440**	1	**-0.429**	**0.511**	0.045	-0.230
MSAVI2- FL	**0.656**	**-0.429**	1	-0.304	-0.362	-0.305
NDMI-Dry	**-0.494**	**0.511**	-0.304	1	-0.007	0.126
MSAVI2- FL to Non-FL	-0.055	0.045	-0.362	-0.007	1	-0.056
NDVI- FL to Non- FL	**-0.433**	-0.230	-0.305	0.126	-0.056	1

Values in bold are different from 0 with a significance level alpha=0.05

These correlation patterns show links between vegetation health, forest cover, dryness, and temperature extremes in Amedi District. Negative associations of NDVI-(FL)with LST-High and NDMI-Dry suggest that forests buffer against high temperatures and aridity. Dense forest cover provides shade, improves soil moisture retention, and regulates microclimates, mitigating dryness and extreme temperatures. Healthy forest

ecosystems stabilize local climates and reduce heat stress impacts. Hotter surface conditions often overlap with dry areas. Increased land surface temperature accelerates evapotranspiration, depleting soil moisture. The strong correlation between NDVI- (FL) and MSAVI2-(FL) supports these indices as tools for assessing forest health(Mohammad et al., 2025).

3.10. Results of ARIMA Modeling for NDVI-Forest Land

The ARIMA model analyzed NDVI-(FL) over time in Figure 11 and assessed its performance using various statistics. Model performance was strong, with the sum of squared errors (SSE) of 112,943.3, a mean squared error (MSE) of 4706.0, and a root mean square error (RMSE) of 68.6, indicating a relatively small average deviation from observed values. The residual white noise variance (4706.0) closely matched the MSE, confirming that the residuals follow a near-random pattern. The mean absolute percentage error (MAPE) was only 2.4%, reflecting high accuracy in model fitting. This indicates that the ARIMA model possesses the capability to generate fairly precise forecasts for immediate trends. The model's log-likelihood (-2Log(Like)) recorded a value of 273.2, while the Final Prediction Error (FPE) was calculated at 5115.2. The selection criteria metrics included the Akaike Information Criterion (AIC) = 277.2, Corrected Akaike Information Criterion (AICC) = 277.8, and Schwarz Bayesian Criterion (SBC) = 279.6 were consistent and stable, and the model converged after four iterations. The fitted ARIMA series closely tracked the historical NDVI-Forest Land trend (2000–2024), which shows a consistent decline, particularly after 2013. Forecasts for 2025-2035 suggest a stabilization and slight recovery of NDVI-Forest Land, indicating that the sharp downward trajectory observed in the past decades may level off in the near future. While this forecast provides a statistically robust projection, it should be interpreted with caution, as ARIMA models capture temporal patterns but do not explicitly account for external ecological drivers such as land-use policies, fire events, or climate change. The ARIMA model works well for short-term NDVI-(FL) forecasting, but as uncertainty increases, it shows limits in long-term projections. According to Huebner, Al-Quraishi, *et al.*(2022)., the model supports a trend toward declining forest cover that is in line with observed increases in temperature and aridity.

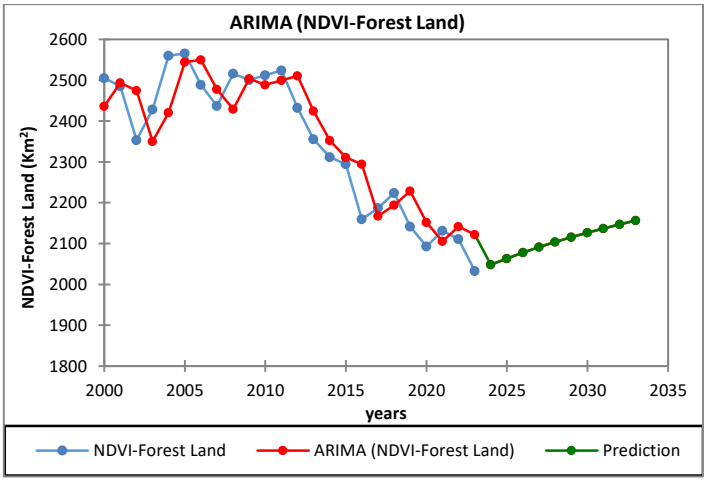

Figure 11: ARIMA Modeling for NDVI-Forest Land.

3.11. Results of ARIMA Modeling for NDMI-Dry

In Figure 12, NDMI-Dry trends across time were analyzed using the ARIMA model, and a range of goodness-of-fit measures were used to assess the model's effectiveness.

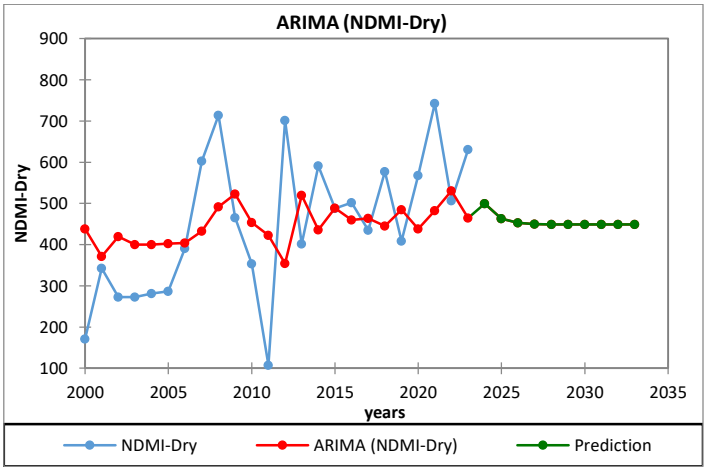

Figure 12: ARIMA Modeling for NDMI-Dry.

The model was developed based on 24 observations, with 22 DF remaining post-parameter estimation. The SSE was 626,150.1, with a MSE of 26,089.6 and a RMSE of 161.5, indicating that, on average, predictions deviate from actual values by about 160 units. The white noise variance (26,089.6) shows the level of

unexplained variability left in the residuals. MAPE was 41.5%, which is relatively high. This suggests that the NDMI-Dry model fits the data better. The model's log-likelihood (-2Log(Like)) recorded a value of 312.3, with AIC = 316.3, AICC = 316.8, and SBC = 318.6, which are again pointing to a comparatively better fit. The ARIMA model for NDMI-Dry adeptly captures the escalating trend of aridity over time. The minimal SSE, MSE, and RMSE values signify the model's strong fit to the data, while the negligible MAPE values indicate precise short-term forecasting accuracy. The ARIMA forecast suggests a continual rise in NDMI-Dry values, indicating an impending expansion of dry conditions. This concurs with prior research indicating an inverse relationship between NDMI-Dry and NDVI/MSAVI2-Forest Land, implying that increasing aridity likely contributes to forest degradation and ecological strain. Furthermore, the positive correlation between NDMI-Dry and LST-High (45-50°C) further bolsters the notion that escalating land surface temperatures may exacerbate dryness. The ARIMA model provides a reliable short-term forecast for NDMI-Dry but becomes less reliable for long-term predictions due to increasing uncertainty. Dry conditions will continue to intensify, with implications for vegetation health, soil moisture retention, and land degradation. Future forecasting models should integrate climate data, precipitation trends, and land-use changes to improve predictive accuracy(Zhang and Zhou, 2016).

3.12. Results of ARIMA Modeling for NDVI-(FL)to Non-Forest Land

The ARIMA model was applied to NDVI-(FL) to Non-(FL) in Figure 13. The model utilized 24 observations, with 22 DF available after parameter estimation. The model achieved an SSE of 54,335.8, MSE of 2264.0, and RMSE of 47.6, with residual variance equal to the MSE, suggesting white noise residuals. However, the MAPE was 68.3%, reflecting difficulties in accurately modeling the large interannual fluctuations. Model selection criteria (AIC = 257.5, AICC = 258.1, SBC = 259.9) were consistent, though convergence required 16 iterations.

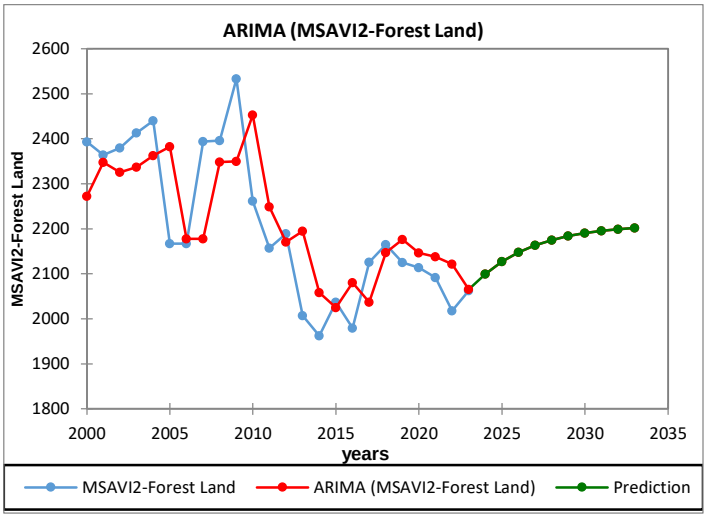

Figure 13: ARIMA Modeling for MSAVI2-Forest Land

ARIMA forecast graph shows (FL)conversion to non-(FL)increasing over time, indicating an ongoing decline in forest area likely due to deforestation, land conversion for agriculture, or Forest fire. The findings show NDVI-(FL) negatively correlated with NDMI-Dry and LST-High (45-50°C), indicating rising temperatures and dryness contribute to forest loss. Environmental factors and human-induced land-use changes drive the transition from (FL)to non-forest land. The ARIMA model forecasts NDVI-(FL)to Non-(FL)conversion with a clear increasing trend in the short term. Long-term forecasts should be interpreted cautiously due to widening uncertainty.

3.13. Results of ARIMA Modeling for MSAVI2-Forest Land

The ARIMA model was utilized for MSAVI2-(FL) in Figure 14, and its efficacy was evaluated through essential goodness-of-fit metrics. The model was trained on 24 observations, resulting in 22 DF post parameter estimation. The model produced an SSE of 283,252.6, MSE of 11,802.2, and RMSE of 108.6. The residual variance equaled the MSE, confirming a near-white noise pattern in residuals. The MAPE was 3.9%, demonstrating a high level of accuracy. Model selection criteria (AIC = 297.9, AICC = 298.5, SBC = 300.3) were consistent, and convergence was reached after 12 iterations. The ARIMA series effectively tracked the historical MSAVI2–Forest Land trend, which showed overall decline from

2000 to 2020, followed by stabilization. Forecasts for 2025–2035 suggest a slight recovery and leveling off, consistent with NDVI-based projections. This indicates that forest cover loss may slow in the near future, though the prediction should be interpreted with caution since ARIMA captures temporal patterns but not external ecological or policy drivers.

Rising temperatures and increased aridity are likely important factors in this trend, as higher temperatures accelerate evapotranspiration and reduce soil moisture, which negatively affects vegetation health. Additionally, the expansion of Non- Forest Land, as shown by previous correlations between NDVI/MSAVI2-Forest Land to Non-Forest Land, suggests that changes in land use and deforestation may be speeding up the degradation of forests. The forecast graph shows a declining trend in MSAVI2-Forest Land, indicating a continuous loss of forested areas over time, which is consistent with earlier studies that showed a negative correlation between MSAVI2-(FL) and LST-High (45-50°C) and NDMI-Dry. Rising temperatures and increased aridity are likely important factors in this trend, as higher temperatures accelerate evapotranspiration and reduce soil moisture, which negatively affects vegetation health (Peñuelas and Sardans, 2021). Additionally, the expansion of non-forest land, as shown by previous correlations between NDVI/MSAVI2-(FL) to Non-Forest Land, suggests that changes in land use and deforestation may be speeding up the degradation of forests. The ARIMA model provides a reliable short-term forecast for MSAVI2-Forest Land, showing a declining trend in forest coverage.

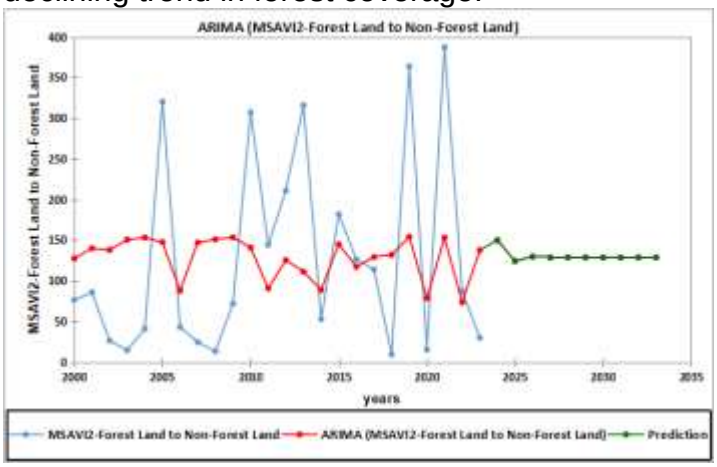

Figure 14: ARIMA Modeling for MSAVI2-Forest Land to Non-FL

3.14. Results of ARIMA Modeling for LST-High (45-50°C)

Figure 15 used the ARIMA model to examine LST-High (45–50°C) trends across time. The estimate of parameters with 22 DF was made possible by the model's training on 24 data sets. The model's error statistics indicate limited accuracy: the SSE was 952,533.3, with a MSE of 39,688.9 and a RMSE of 199.2, showing that, on average, predictions deviate by about 200 units from the observed values. The white noise variance (39,688.9) confirms that a large portion of the data's variability was not captured by the model. The MAPE was 159.5%, which is very high, meaning forecasts deviate on average by more than one and a half times the actual values. Likelihood-based criteria also suggest a weak fit: −2 Log Likelihood = 322.3, with information criteria values of AIC = 326.3, AICC = 326.8, and SBC = 328.6, all relatively large. The model converged after 14 iterations, so it is stable but not highly accurate. Overall, while ARIMA provides a smoothed representation of the data and a flat prediction trend for 2024–2033, the high error values highlight that it does not adequately capture the strong fluctuations present in the actual time series.

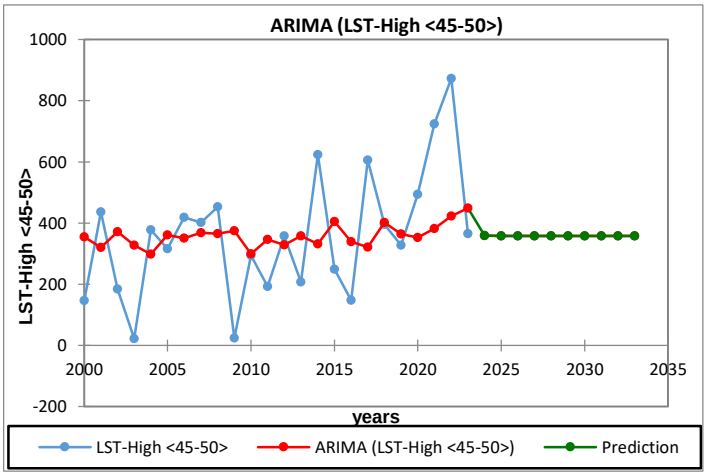

Figure 15: ARIMA Modeling for LST-High (45-50°C)

The ARIMA model adeptly captures the historical trend of LST-High (45-50°C), showcasing robust predictive capabilities with minimal forecasting errors. The model's low SSE, MSE, and RMSE values validate its strong fit to the data. The projected graph for LST-High (45-50°C) displays a discernible upward trajectory,

hinting at the potential expansion of high land surface temperature regions over time. This observation is consistent with previous research indicating a negative correlation between LST-High (45-50°C) and NDVI-(FL) (-0.440) as well as MSAVI2-(FL) (-0.429), suggesting that escalating temperatures contribute to vegetation stress and forest depletion. Furthermore, the strong positive correlation between LST-High (45-50°C) and NDMI-Dry (0.511) suggests that deforestation leads to an increase in temperatures.

3.15. Interpretation of the Principal Component Analysis (PCA) Biplot

The PCA biplot depicted in Figure 16 offers a visual representation of the interconnections between environmental and land-use variables, with F1 (48.41%) and F2 (18.37%) collectively elucidating 66.79% of the overall variance. This indicates that the initial two principal components encapsulate a substantial portion of the dataset's variability, rendering this analysis valuable for comprehending fundamental patterns. Variables that are closely situated exhibit a robust positive correlation, whereas those diverging in opposite directions demonstrate a negative correlation.

One of the most striking patterns in the biplot is the opposing directions of NDVI-(FL) and MSAVI2-(FL) against NDMI-Dry and LST-High (45-50°C), indicating a strong negative correlation. As dryness and land surface temperature increase, (FL)cover decreases. Variables further from the origin contribute more to explained variance, highlighting the impact of climate stressors on vegetation decline. The robust correlation between NDVI-(FL) to Non-(FL) and MSAVI2-(FL)to Non-(FL)underscores an ongoing process of land conversion, wherein forested areas are transitioning into non-forest terrain. This trend indicates that deforestation leads to forest depletion. The negative correlation between forested land and land conversion parameters suggests that as forests diminish, non-forest areas expand, highlighting the magnitude of landscape transformation. The adverse projection of NDVI/MSAVI2-(FL) against NDMI-Dry and LST-High (45-50°C) implies that forest degradation is intricately linked to escalating temperatures and arid conditions. This pattern validates prior research, indicating the high susceptibility of forests to climatic stressors. As temperatures rise and moisture levels decrease, forest vitality deteriorates, resulting in diminished forest coverage. The close association between NDMI-Dry and LST-High (45-50°C) further bolsters the proposition that heat, Forest fire, forest cutting and aridity hasten vegetation loss, heightening susceptibility to land degradation(Li et al., 2023).

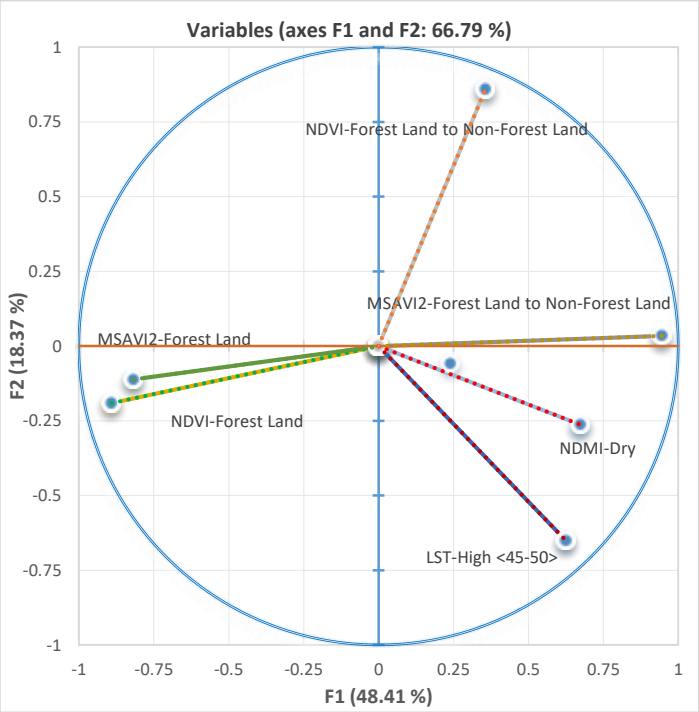

Figure 16: Principal Component Analysis (PCA) Biplot of Vegetation Indices, LST-High (<45–50°C), NDMI-Dry, and Forest/Non-Forest Variables.

The PCA biplot strongly reinforces the earlier correlation findings, underscoring the inverse correlation between forested land and environmental stressors such as high temperatures and dryness. The juxtaposition of NDVI/MSAVI2-(FL) opposite to NDMI-Dry and LST-High (45-50°C) highlights the high sensitivity of forests to temperature and moisture fluctuations. This indicates that climatic elements play a pivotal role in determining forest resilience, with heat stress and dry conditions expediting forest decline.

Another key observation is the grouping of similar variables, confirming relationships found in correlation analysis. NDVI-(FL) and MSAVI2-

(FL)align closely, indicating consistent measurement of forest land. NDVI-(FL) to Non-(FL) and MSAVI2-(FL)to Non-(FL)cluster together in the opposite direction of forest indices, emphasizing their role in land conversion. NDMI-Dry and LST-High (45-50°C) extend in the same direction, suggesting that higher land surface temperatures are linked to increased dryness, likely contributing to forest loss(Le et al., 2023). Moreover, the pronounced clustering of NDVI-(FL) to Non-(FL) and MSAVI2-(FL)to Non-(FL)suggests that alterations in land use are a predominant driver of forest loss. The projection along the F1 axis, capturing nearly 50% of the variance, indicates that deforestation and land conversion are principal structuring influences in landscape dynamics. This finding underscores the significance of addressing anthropogenic land alterations to mitigate forest degradation. Subsequent research should integrate climate forecasts, socio-economic determinants, and policy ramifications to formulate effective conservation strategies. It will be imperative to address both environmental and human-induced stressors on forests to uphold biodiversity, ecosystem equilibrium, and climate resilience.

4. Conclusion

This study provides a comprehensive assessment of forest degradation in the Amedi District of Duhok Province, Iraq, from 2000 to 2024 using multi-temporal satellite data and advanced statistical modeling. The analysis of NDVI, MSAVI2, LST, and NDMI reveals a consistent and statistically significant decline in forest cover, paralleled by increasing land surface temperatures and expanding dry zones. NDVI-derived forest land dropped from 90.3% to 73.3%, while MSAVI2-based estimates show a similar reduction. Non-forest areas expanded markedly, indicating a clear land conversion trend. Time series modeling using ARIMA confirms the persistence of this degradation, with forecasts projecting continued decline beyond 2024. Trend detection through the Mann-Kendall test and Sen's slope estimation confirmed these findings, while strong correlations ($r > 0.7$, $p < 0.05$) between vegetation indices and environmental stressors highlight the role of climate variability in accelerating forest loss. The correlation and PCA analyses further validate that areas with higher forest health are associated with lower temperatures and moisture deficits, emphasizing the buffering role of forest ecosystems. The results underscore the importance of sustained forest monitoring through remote sensing to track ecological changes and assess the effectiveness of land management policies. Conservation strategies should prioritize the integration of high-resolution satellite data with predictive models like ARIMA to enhance early warning systems and guide adaptive responses. Strengthening forest management practices and implementing targeted conservation policies will be essential to mitigate future forest loss and maintain ecosystem stability in the face of ongoing climatic and anthropogenic pressures.

5. Recommendations

1. Implement robust conservation policies to reduce deforestation. Enhance reforestation and restoration projects to recover degraded lands with native species for ecosystem stability and soil moisture retention.
2. Encourage land-use planning for sustainable agriculture and urban development. Use agroforestry and buffer zones to reduce the impacts of urban expansion and land conversion, preserving forest cover.
3. Develop measures to counteract rising land surface temperatures and increasing aridity. Adopt water conservation techniques, enhance soil moisture practices, and implement urban greening initiatives. Reduce local heat island effects.
4. Utilize remote sensing and time-series modeling tools like ARIMA to monitor changes in forest cover, temperature, and moisture. Ongoing monitoring provides data for policy interventions and adapting management strategies.
5. Engage communities, stakeholders, and policymakers in conservation efforts by raising awareness about the benefits of healthy forest ecosystems. Educational campaigns and participatory management can foster a commitment to sustainable land practices.
6. Support interdisciplinary research integrating climate forecasts, socio-economic factors, and

land-use dynamics to develop holistic conservation strategies. Collaboration among agencies, institutions, and communities is essential to address stressors on forest ecosystems.

Author Contributions: Conceptualization, N.M.A, M. H. and H.A.A.G.; Data curation, N.M.A, M. H. And H.A.A.G.; Formal analysis, N.M.A, M. H. and H.A.A.G.; Investigation, N.M.A, M. H. and H.A.A.G.; Methodology, N.M.A, M. H. and H.A.A.G.; Resources, N.M.A and..; Supervision, M. H. and H.A.A.G.; Validation, N.M.A.; Visualization, N.M.A., M. H. and H.A.A.G.; Writing—original draft, N.M.A.; Writing—review and editing, M. H. and H.A.A.G. All authors have read and agreed to the published version of the manuscript.

Acknowledgement: The authors would like to thank the United States Geological Service (USGS) for providing the Landsat images freely on its website. We are extremely grateful to the anonymous reviewers for their insightful comments and suggestions that significantly enhanced the quality of our paper. Department of Forestry, and College of Agricultural Engineering Sciences, University of Duhok, Department of Forestry, College of Agriculture Engineering Sciences, Salahaddin University-Erbil, for their valuable support.

Financial support: This study has received partial funding from the College of Agricultural Engineering Sciences, University of Duhok, and Salahaddin University Kurdistan Region, Iraq.

Potential conflicts of interest. The authors declare no conflict of interest.

Appendix Table A1. Inventory and Field Data Validation for Amedi District's Native Forest (Plot Size: 50X50)

Plot ID:	Landcover Type	Coordinates		
		Latitude	Longitude	Altitude (m)
Plot1	Deciduous Forest	N 37°10'59.7''	E 43°18'35.4''	918
Plot2	Mixed Forest	N 37°01'24.5''	E 43°15'27.0''	967
Plot3	Deciduous Forest	N 37°04'14.1''	E 43°35'18.1''	767
Plot4	Mixed Forest	N 37°04'03.9''	E 43°37'13.1''	757
Plot5	Deciduous Forest	N 36°55'47.2''	E 43°25'32.8''	959
Plot6	Deciduous Forest	N 37°04'54.2''	E 43°16'01.5''	956
Plot7	Deciduous Forest	N 37°06'30.2''	E 43°13'07.4''	1013
Plot8	Deciduous Forest	N 37°08'54.2''	E 43°10'14.4''	1112
Plot9	Deciduous Forest	N 37°09'53.7''	E 43°09'12.2''	1258
Plot10	Deciduous Forest	N 37°11'00.1''	E 43°11'16.3''	1054
Plot11	Deciduous Forest	N 37°09'53.7''	E 43°09'12.2''	1258
Plot12	Deciduous Forest	N 37°11'00.1''	E 43°11'16.3''	1054
Plot13	Deciduous Forest	N 37°12'54.8''	E 43°13'05.1''	886
Plot14	Deciduous Forest	N 37°13'15.8''	E 43°11'56.4''	873
Plot15	Deciduous Forest	N 37°10'59.4''	E 43°11'16.3''	1069
Plot16	Mixed Forest	N 37°01'02.8''	E 43°18'29.2''	1162
Plot17	Deciduous Forest	N 37°02'04.2''	E 43°24'42.8''	983
Plot18	Deciduous Forest	N 37°04'36.2''	E 43°12'16.2''	820
Plot19	Deciduous Forest	N 37°09'24.6''	E 43°09'17.5''	1257
Plot20	Deciduous Forest	N 37°06'45.8''	E 43°18'40.4''	1215
Plot21	Deciduous Forest	N 37°10'33.2''	E 43°11'35.5''	1217
Plot22	Mixed Forest	N 37°10'26.5''	E 43°14'28.7''	1208
Plot23	Deciduous Forest	N 37°10'47.4''	E 43°17'40.8''	911
Plot24	Deciduous Forest	N 37°12'11.9''	E 43°19'23.1''	1034
Plot25	Deciduous Forest	N 37°13'05.4''	E 43°23'16.3''	1259
Plot26	Deciduous Forest	N 37°14'57.5''	E 43°22'05.2''	1508
Plot27	Deciduous Forest	N 37°15'01.16''	E 43°25'02.0''	1346
Plot28	Mixed Forest	N 37°11'25.2''	E 43°31'00.8''	1054
Plot29	Deciduous Forest	N 37°14'02.4''	E 43°30'08.8''	1714
Plot30	Deciduous Forest	N 37°05'51.6''	E 43°25'49.6''	1104
Plot31	Mixed Forest	N 37°06'03.6''	E 43°27'18.9''	1175
Plot32	Deciduous Forest	N 37°02'29.2''	E 43°42'24.0''	626
Plot33	Evergreen Forest	N 37°01'39.6''	E 43°47'51.6''	608

References

Abdalkarim, K.O., Gaznayee, H.A.A., Al-quraishi, A.M.F., 2023. Predictive Digital Mapping of Surface Soil Properties using Remote Sensing and Multivariate Statistical Analysis . ZANCO J. Pure Appl. Sci. 35, 189–203.

Abdulwahid, M.Y., Galobardes, I., Radoine, H., 2021. Understanding the use of timber in semi-arid regions: Kurdistan region of iraq, a case study. Sustain. 13, 1–14.

Anyamba, A., Tucker, C.J., 2012. Historical perspectives on AVHRR NDVI and vegetation drought monitoring. Remote Sens. Drought Innov. Monit. Approaches 23–49.

Aquino, D. do N., Neto, O.C. da R., Moreira, M.A., Teixeira, A. dos S., de Andrade, E.M., 2018. Use of remote sensing to identify areas at risk of degradation in the semi-arid region. Rev. Cienc. Agron. 49, 420–429.

Atilgan, A., Tanriverdi, C., Yucel, A., Hasan, O., and Degirmenci, H., 2017. Analysis of Long-Term Temperature Data Using Mann-Kendall Trend Test and Linear Regression Methods: the Case of the Southeastern Anatolia Region. Sci. Pap. a-Agronomy 60, 455–462.

Basu, J.P., 2011. Working Paper No . 2011 / 14 Adaptation to climate change , Vulnerability and Micro- Insurance Business : A Study on Forest Dependent Communities in Drought prone areas of West Bengal , India. Work. Pap. No. 2011/14 Adapt. 1–40.

Beg, A.A.F., Al-Sulttani, A.H., 2020. Spatial assessment of drought conditions over Iraq using the standardized precipitation index (SPI) and GIS techniques. Environ. Remote Sens. GIS Iraq 447–462.

Bohlmann, U.M., Koller, V.F., 2020. ESA and the Arctic-The European Space Agency's contributions to a

sustainable Arctic. Acta Astronaut. 176, 33–39.
Borrelli, P., Robinson, D.A., Panagos, P., Lugato, E., Yang, J.E., Alewell, C., Wuepper, D., Montanarella, L., Ballabio, C., 2020. Land use and climate change impacts on global soil erosion by water (2015-2070). Proc. Natl. Acad. Sci. U. S. A. 117, 21994–22001.
Bousquet, E., Mialon, A., Rodriguez-Fernandez, N., Mermoz, S., Kerr, Y., 2022. Monitoring post-fire recovery of various vegetation biomes using multi-wavelength satellite remote sensing. Biogeosciences 19, 3317–3336.
Congalton, R.G., Green, K., 2019. Assessing the accuracy of remotely sensed data: principles and practices. CRC press.
Corps, U.S.A., Lukas, R., 2005. Mann-Kendall Analysis Mann-Kendall Analysis for the Fort Ord Site. Hydrogeol. Inc. – OU-1 Annu. Groundw. Monit. Rep. – Former Fort Ord, Calif.
Dash, P., Göttsche, F.M., Olesen, F.S., Fischer, H., 2002. Land surface temperature and emissivity estimation from passive sensor data: Theory and practice-current trends. Int. J. Remote Sens. 23, 2563–2594.
Donglian Sun, and M.K., 2007. Note on the NDVI-LST relationship and the use of temperature-related drought indices over North America. Geophys. Res. Lett. 34, 1–4.
ECMWF, G., 2020. European centre for medium-range weather forecasts, ECMWF.
Eklund, L., 2012. Migration Patterns in Duhok Governorate, Iraq, 2000-2010. Open Geogr. J. 5, 48–58.
Eklund, L., Seaquist, J., 2015. Meteorological, agricultural and socioeconomic drought in the Duhok Governorate, Iraqi Kurdistan. Nat. Hazards 76, 421–441.
El Chami, D., El Moujabber, M., 2024. Sustainable Agriculture and Climate Resilience. Sustain. 16, 1–7.
Elsa Sattout, E.S., Salma Talhouk, S.T., Nader Kabbani, N.K., 2005. Lebanon. In: Valuing Mediterranean Forests: Towards Total Economic Value. CABI Publishing Wallingford UK, pp. 161–175.
Field, A., 2024. Discovering statistics using R. Sage Publ. limited; 2024 Feb 22. 50, 50-2114-50–2114.
Gabriele, M., Brumana, R., Previtali, M., Cazzani, A., 2023. A combined GIS and remote sensing approach for monitoring climate change-related land degradation to support landscape preservation and planning tools: the Basilicata case study, Applied Geomatics. Springer Berlin Heidelberg.
Gaznayee, Heman Abdulkhaleq A, Al-quraishi, A.M.F., Mahdi, K., Messina, J.P., Zaki, S.H., Razvanchy, H.A.S., Hakzi, K., Huebner, L., Ababakr, S.H., Riksen, M., Ritsema, C., 2022. Drought Severity and Frequency Analysis Aided by Spectral and Meteorological Indices in the Kurdistan Region of Iraq. Water 14, 1–29.
Gaznayee, Heman Abdulkhaleq A., Al-Quraishi, A.M.F., Mahdi, K., Ritsema, C., 2022. A Geospatial Approach for Analysis of Drought Impacts on Vegetation Cover and Land Surface Temperature in the Kurdistan Region of Iraq. Water 14, 927.
Ghahraman, B., Sepaskhah, A.R., 2004. Linear and non-linear optimization models for allocation of a limited water supply. Irrig. Drain. 53, 39–54.
Gholamnia, M., Khandan, R., Bonafoni, S., Sadeghi, A., 2019. Spatiotemporal analysis of MODIS NDVI in the semi-arid region of Kurdistan (Iran). Remote Sens. 11, 8–12.
Gilbert, R.O., 1987. Statistical Methods for Environmental Pollution Monitoring. Stat. Methods Environ. Pollut. Monit. 204–224.
Gu, Y., Hunt, E., Wardlow, B., Basara, J.B., Brown, J.F., Verdin, J.P., 2008. Evaluation of MODIS NDVI and NDWI for vegetation drought monitoring using Oklahoma Mesonet soil moisture data. Geophys. Res. Lett. 35, 1–5.
Habeeb, H.N., Mustafa, Y.T., 2024. Deep Learning-Based Prediction of Forest Cover Change in Duhok, Iraq: Past and Future. Forestist 75.
Hamad, R., Balzter, H., Kolo, K., 2017. Multi-Criteria Assessment of Land Cover Dynamic Changes in Halgurd Sakran National Park (HSNP), Kurdistan Region of Iraq, Using Remote Sensing and GIS. Land 6, 18.
Hamed, K.H., 2008. Trend detection in hydrologic data: The Mann-Kendall trend test under the scaling hypothesis. J. Hydrol. 349, 350–363.
Hansen, M.C., Potapov, P. V, Moore, R., Hancher, M., Turubanova, S.A., Tyukavina, A., Thau, D., Stehman, S. V, Goetz, S.J., Loveland, T.R., 2013. High-resolution global maps of 21st-century forest cover change. Science (80-.). 342, 850–853.
Hassan, Z.M., Al-Jiboori, M.H., Al-Abassi, H.M., 2020. The Effect of The Extremes Heat Waves on Mortality Rates in Baghdad During the Period (2004-2018). Al-Mustansiriyah J. Sci. 31, 15–23.
Huebner, L., Al-Quraishi, A.M.F., Branch, O., Gaznayee, H.A.A., 2022a. Sahel Afforestation and Simulated Risks of Heatwaves and Flooding Versus Ecological Revegetation That Combines Planting and Succession. J. Geosci. Environ. Prot. 10, 94–108.
Huebner, L., Fadhil Al-Quraishi, A.M., Branch, O., Gaznayee, H.A.A., 2022b. New approaches: Use of assisted natural succession in revegetation of inhabited arid drylands as alternative to large-scale afforestation. SN Appl. Sci. 4.
Hyndman, R.J., Athanasopoulos, G., 2018. Forecasting : Principles and Practice.
Isbaex, C., Coelho, A.M., 2021. The potential of Sentinel-2 satellite images for land-cover/land-use and forest biomass estimation: A review. IntechOpen.
Ismael, S.Y., 2015. Promoting integrated heritage conservation and management in Iraqi Kurdistan Region: Applicability of values-based approach the case study of Akre and Amedy City in Duhok Province.
Jaff, D., 2023. Conflict, environmental destruction and climate change: a tragedy in Iraq that demands action. Med. Confl. Surviv. 39, 162–171.
Kahya, E., Kalayci, S., 2004. Trend analysis of streamflow in Turkey. J. Hydrol. 289, 128–144.

Kalluri, S., Cao, C., Heidinger, A., Ignatov, A., Key, J., Smith, T., 2021. The advanced very high resolution radiometer contributing to earth observations for over 40 years. Bull. Am. Meteorol. Soc. 102, E351–E366.

Kamusoko, C., 2022. Land Cover Classification Accuracy Assessment. Springer Geogr. 80, 105–118.

Kim, S., Ali, A.M., Kim, S., Bayatvarkeshi, M., Muhammad, A., Ahmed, K., 2024. Decadal Climate and Landform Variables Analysis in Iraq Using Remote Sensing Datasets Decadal Climate and Landform Variables Analysis in Iraq Using Remote Sensing Datasets. AUIQ Tech. Eng. Sci. 2024;142–55 1.

Köhl, M., Lasco, R., Cifuentes, M., Jonsson, Ö., Korhonen, K.T., Mundhenk, P., de Jesus Navar, J., Stinson, G., 2015. Changes in forest production, biomass and carbon: Results from the 2015 UN FAO Global Forest Resource Assessment. For. Ecol. Manage. 352, 21–34.

Kollert, W., Carle, J., Rosengren, L., 2014. Poplars and willows for rural livelihoods and sustainable development. In: Poplars and Willows: Trees for Society and the Environment. CABI Wallingford UK, pp. 577–602.

Kumar, R., Kumar, A., Saikia, P., 2022. Deforestation and Forests Degradation Impacts on the Environment BT - Environmental Degradation: Challenges and Strategies for Mitigation. In: Singh, V.P., Yadav, S., Yadav, K.K., Yadava, R.N. (Eds.), . Springer International Publishing, Cham, pp. 19–46.

Le, T.S., Harper, R., Dell, B., 2023. Application of Remote Sensing in Detecting and Monitoring Water Stress in Forests. Remote Sens. 15.

Li, T., Cui, L., Liu, L., Chen, Y., Liu, H., Song, X., Xu, Z., 2023. Advances in the study of global forest wildfires. J. Soils Sediments 23, 2654–2668.

Li, Z.L., Tang, B.H., Wu, H., Ren, H., Yan, G., Wan, Z., Trigo, I.F., Sobrino, J.A., 2013. Satellite-derived land surface temperature: Current status and perspectives. Remote Sens. Environ. 131, 14–37.

Liu, J.J., Kestell, P., Findlay, M., Riley, G., Ackland, S., Simpson, A., Isaacs, R., McKeage, M.J., 2004. Application of liquid chromatography-mass spectrometry to monitoring plasma cyclophosphamide levels in phase I trial cancer patients. Clin. Exp. Pharmacol. Physiol. 31, 677–682.

Liu, Z., He, C., Zhou, Y., Wu, J., 2014. How much of the world's land has been urbanized, really? A hierarchical framework for avoiding confusion. Landsc. Ecol. 29, 763–771.

Mathbout, S., Boustras, G., Papazoglou, P., Martin Vide, J., Raai, F., 2025. Integrating climate indices and land use practices for comprehensive drought monitoring in Syria: Impacts and implications. Environ. Sustain. Indic. 26.

Mohammad, R.K., Lojka, B., 2018. Farmers ' Use and Preferences of Trees in Kurdistan Region of Iraq.

Mohammad, R.K., Zaki, S.H., Gaznayee, H.A.A., Sabr, H.A., Aliehsan, P.H., Sherwan, Y., Ababakr, S.H., Razvanchy, H.A., Hakzi, K.K., Region, K., 2025. ASSESSING DROUGHT IMPACTS IN ERBIL , IRAQI KURDISTAN : A STUDY OF LAND SURFACE TEMPERATURE AND VEGETATION HEALTH INDEX USING LANDSAT TIME- 13, 88–96.

Mustafa, Y.T., Noori, M.J., 2013. Satellite remote sensing and geographic information systems (GIS) to assess changes in the water level in the Duhok dam. Int. J. Water Resour. Environ. Eng. 5, 351–359.

Nations, U., 2010. G LOBAL F OREST R ESOURCES A SSESSMENT 2010 C OUNTRY R EPORT.

Nemani, R.R., Keeling, C.D., Hashimoto, H., Jolly, W.M., Piper, S.C., Tucker, C.J., Myneni, R.B., Running, S.W., 2003. Climate-driven increases in global terrestrial net primary production from 1982 to 1999. Science (80-.). 300, 1560–1563.

Niro, F., Goryl, P., Dransfeld, S., Boccia, V., Gascon, F., Adams, J., Themann, B., Scifoni, S., Doxani, G., 2021. European Space Agency (ESA) calibration/validation strategy for optical land-imaging satellites and pathway towards interoperability. Remote Sens. 13, 3003.

O'Brien, R.M., 2007. A caution regarding rules of thumb for variance inflation factors. Qual. Quant. 41, 673–690.

Ozturk, T., Turp, M.T., Türkeş, M., Kurnaz, M.L., 2017. Projected changes in temperature and precipitation climatology of Central Asia CORDEX Region 8 by using RegCM4. 3.5. Atmos. Res. 183, 296–307.

Partal, T., Kahya, E., 2006. Trend analysis in Turkish precipitation data. Hydrol. Process. 20, 2011–2026.

Peñuelas, J., Sardans, J., 2021. Global change and forest disturbances in the mediterranean basin: Breakthroughs, knowledge gaps, and recommendations. Forests 12, 1–27.

Pettorelli, N., Vik, J.O., Mysterud, A., Gaillard, J.M., Tucker, C.J., Stenseth, N.C., 2005. Using the satellite-derived NDVI to assess ecological responses to environmental change. Trends Ecol. Evol. 20, 503–510.

Pohlert, T., 2016. Package ' trend ': Non-Parametric Trend Tests and Change-Point Detection. R Packag. 26.

Qi, J, Kerr, Y., Chehbouni, A., 1994. External factor consideration in vegetation index development. Proc. 6th Int. Symp. Phys. Meas. Signatures Remote Sensing, ISPRS 723–730.

Qi, Jiaguo, Kerr, Y., Chehbouni, A., 1994. External factor consideration in vegetation index development. Proc. Phys. Meas. Signatures Remote Sens. 723–730.

Qutbudin, I., Shiru, M.S., Sharafati, A., Ahmed, K., Al-Ansari, N., Yaseen, Z.M., Shahid, S., Wang, X., 2019. Seasonal Drought Pattern Changes Due to Climate Variability: Case Study in Afghanistan. Water 11, 1096.

Resources, 2019. Review of the Agricultural Sector In The Kurdistan Region Of Iraq: Analysis On Crops, Water Resources And Irrigation, And Selected Value Chains. Annu. Rport.

Roy, D.P., Jin, Y., Lewis, P.E., Justice, C.O., 2005. Prototyping a global algorithm for systematic fire-affected area mapping using MODIS time series data. Remote Sens. Environ. 97, 137–162.

Roy, D.P., Kovalskyy, V., Zhang, H.K., Vermote, E.F., Yan, L., Kumar, S.S., Egorov, A., 2016. Characterization of Landsat-7 to Landsat-8 reflective wavelength and normalized difference vegetation index continuity. Remote Sens. Environ. 185, 57–70.

Roy, D.P., Wulder, M.A., Loveland, T.R., Woodcock, C.E., Allen, R.G., Anderson, M.C., Helder, D., Irons, J.R., Johnson, D.M., Kennedy, R., 2014. Landsat-8: Science and product vision for terrestrial global change research. Remote Sens. Environ. 145, 154–172.

Schmidt, C., 2017. Remote Sensing of Drought. Natl. Aeronaut. Sp. Adm. Appl. Remote Sens. Train. http//arset.gsfc.nasa.gov.

Seymour, L., Brockwell, P.J., Davis, R.A., 1997. Introduction to Time Series and Forecasting., Journal of the American Statistical Association.

SUHET, 2015. EL-2 User Handbook Sentinel-2 User Handbook. Ind. Eng. Chem. 48, 1404–1406.

Sun, Q., Tan, J., Xu, Y., 2009. An ERDAS image processing method for retrieving LST and describing urban heat evolution: A case study in the Pearl River Delta Region in South China. Environ. Earth Sci. 59, 1047–1055.

Taufik, A., Ahmad, S.S.S., Khairuddin, N.F.E., 2017. Classification of Landsat 8 Satellite Data using Fuzzy c-means. Proc. 2017 Int. Conf. Mach. Learn. Soft Comput. - ICMLSC ’17 58–62.

USGS, 2017. Product guide 1–14.

Vilanova, R.S., Delgado, R.C., da Silva Abel, E.L., Teodoro, P.E., Silva Junior, C.A., Wanderley, H.S., Capristo-Silva, G.F., 2020. Past and future assessment of vegetation activity for the state of Amazonas-Brazil. Remote Sens. Appl. Soc. Environ. 17, 100278.

Wang, Z., Li, Z., Xie, Y., Souza, C., Filho, J.S.S., Pinheiro, S., 2024. AI-based Validation of Deforestation Using High-Resolution Satellite Imagery in the Brazilian Amazon. Int. Arch. Photogramm. Remote Sens. Spat. Inf. Sci. - ISPRS Arch. 48, 583–588.

Zaki, S.H., Gaznayee, H.A.A., Hawez, P.S., 2023. Multi-sensor Satellite Drought Analysis using Landsat and MODIS Time- Series Based on NDVI and Rainfall. ZANCO J. Pure Appl. Sci. 35, 205–2017.

Zhang, D., Zhou, G., 2016. Estimation of soil moisture from optical and thermal remote sensing: A review. Sensors (Switzerland) 16.

Zhao, M., Running, S.W., 2010. Drought-induced reduction in global terrestrial net primary production from 2000 through 2009. Science (80-.). 329, 940–943.

Zhu, Z., Woodcock, C.E., 2012. Object-based cloud and cloud shadow detection in Landsat imagery. Remote Sens. Environ. 118, 83–94.